Master's thesis

NTNU
Norwegian University of Science and Technology
Faculty of Natural Sciences
Department of Materials Science and Engineering

Thea Birgitte Berge

Scale-up of Sonochemical Synthesis of Nanocatalysts for Fuel Cells and Electrolyzers

Master's thesis in Chemical Engineering and Biotechnology
Supervisor: Frode Seland
Co-supervisor: Henrik Erring Hansen
June 2023

NTNU
Norwegian University of
Science and Technology

Thea Birgitte Berge

Scale-up of Sonochemical Synthesis of Nanocatalysts for Fuel Cells and Electrolyzers

Master's thesis in Chemical Engineering and Biotechnology
Supervisor: Frode Seland
Co-supervisor: Henrik Erring Hansen
June 2023

Norwegian University of Science and Technology
Faculty of Natural Sciences
Department of Materials Science and Engineering

NTNU
Norwegian University of
Science and Technology

ABSTRACT

Sammendrag

Hensikten med dette arbeidet var å oppskalere en sonokjemisk synteserute ved bruk av en 346 kHz ultralyd platetransduser for å produsere Pt/XC72 med reproduserbare egenskaper, og høy katalytisk aktivitet for oksygenreduksjonsreaksjonen (ORR) og hydrogenevolusjonsreaksjonen (HER) til brenselcelle og vannelektrolysør applikasjoner. Reduserte katalysator kostnader som følge av oppskalering vil kunne styrke hydrogens posisjon som drivstoff, med det overordnede formålet å redusere miljøpåvirkningene knyttet til forbrenning av fossilt brensel i transportsektoren

Oppskalering ble oppnådd ved å øke reaktorvolumet med 300%, sammenlignet med et mindre reaktorvolum brukt i tidligere arbeider. Den sonokjemiske effektiviteten for å produsere reduksjonsmidler ble opprettholdt for oppskalering av reaktorvolumer. Det ble foreslått at radikaldannelsen ble opprettholdt grunnet dannelse av lik mengde kavitasjonsbobler. Faktorer som påvirker akustisk kavitasjon ble presentert og diskutert, men ytterligere undersøkelser er nødvendig for å få innsikt i hvorfor radikal dannelsen opprettholdes.

Økt effektivitet av oppskaleringen ble oppnådd ved å optimalisere konsentrasjonen av etanol, som øker levetiden til reduksjonsmidlet ved å selv bli omdannet til et radikal av primær radikaler. Ytterligere effektivisering ble oppnådd ved å tilsette XC72 mot slutten av syntesetiden, i stedet for starten, ettersom XC72 demper ultralydbølger og dermed hindrer dannelse av reduksjonsmiddel.

Reproduserbare partikler med en jevn størrelsesfordeling ble funnet ved fysiske karakteriseringsmetoder, og tilskrives det observerte homogene reaksjonsmiljøet av jevnt fordelte radikaler, som kontinuerlig dannes gjennom hele reaktor volumet. De sonokjemisk aktive områdene ble visualisert med sonokjemiskluminescens.

Fysisk karakterisering og voltametriske metoder ble brukt for å måle overflatearealet til Pt. Overflatearealet ble brukt til å beregne strømtettheten for evaluering av katalytisk aktivitet, både med og uten normalisering på Pt mengde. Den høyeste katalytiske aktiviteten for HER og ORR ble oppnådd for syntesene, med XC72 tilsatt mot slutten av syntesetiden.

Abstract

The objective of this work was to scale-up a sonochemical synthesis route using a 346 kHz ultrasonic plate transducer for producing Pt/XC72 with reproducible properties and high catalytic performance towards the oxygen reduction reaction (ORR) and the hydrogen evolution reaction (HER) for fuel cells and electrolyzer applications. The intended outcome is to strengthen hydrogen's position as a fuel by reducing catalyst costs to mitigate environmental impacts associated with the combustion of fossil fuels in the transport sector.

Scale-up was achieved by a 300% increase in reactor volume by extending the reactor height, compared to a small-scale reactor volume used in previous works. The sonochemical efficiency for producing reducing agents was maintained for scale-up reactor volumes. It was suggested that the radical formation was maintained due to approximately the same amount of cavitation bubbles being generated. Multiple factors that affect cavitation bubble formation and collapse were presented. However, further investigation is required to gain insight into the precise mechanisms of why the radical formation is maintained.

Increased efficiency of scale-up was achieved by optimizing the radical scavenger concentration. Further decrease in synthesis time was achieved by adding XC72 near the end of synthesis, as XC72 added from the start hindered radical formation due to the dampening of ultrasonic waves.

Reproducible particles with a narrow size distribution were revealed by physical characterization methods, and are attributed to the observed homogeneous reaction environment of evenly distributed radicals that were continuously generated throughout the reactor. Physical characterization and voltammetric methods were used to measure the surface area of Pt. The surface area was used to calculate the current density, without normalizing on catalyst loading, for assessing the catalytic performance. Reproducible catalytic activity towards the HER and ORR reactions was achieved for most syntheses, further supporting reproducible particle properties observed by physical characterization.

Preface

This master's thesis is written during the spring of 2023 and completes a M.Sc. within Chemical Engineering and Biotechnology with a specialization in Materials Chemistry and Energy Technology at the Department of Materials Science and Engineering at the Norwegian University of Science and Technology. The aim of the project is scale-up of a sonochemical synthesis method for producing platinum nanoparticles as an electrocatalyst for fuel cells and electrolyzes.

I would like to express my sincere gratitude and appreciation to the main supervisor Professor Frode Seland and co-supervisor Henrik Erring Hansen, for their insights and guidance. Special thanks and gratitude go to Henrik for providing instructions on experimental techniques, feedback on manuscripts, and enthusiasm toward sonochemistry. I would like to acknowledge employees at the TEM Gemini Centre in Trondheim, Norway, for conducting transmission electron microscopy (TEM). The Norwegian Fuel Cell and Hydrogen Centre (SINTEF) is acknowledged for providing training for in-situ catalyst testing. The Research Council of Norway is acknowledged for the support to the Norwegian Micro- and Nano-Fabrication Facility, NorFab.

I would like to thank the Department of Materials Science and Engineering employees for providing training on technical instruments and always being willing to help. Thanks are in order to the members of the Electrochemistry Group for academic discussion, feedback, and social gatherings. Finally, I want to express my gratitude to Sander for always being supportive and a true inspiration.

I declare that the work has been performed independently and in accordance with the rules and regulations of the Norwegian University of Science and Technology.

CONTENTS

LIST OF FIGURES

LIST OF TABLES

ABBREVIATIONS

- **BET** Brunauer-Emmett-Teller
- **BEV** Battery Electric Vehicle
- **BF** Bright Field
- **CCM** Catalyst Coated Membrane
- **CE** Counter Electrode
- **CNT** Classical Nucleation Theory
- **CV** Cyclic Voltammetry
- **ECSA** Electrochemical Surface Area
- **EDS** Energy Dispersive X-ray Spectroscopy
- **EIS** Electrochemical Impedance Spectroscopy
- **FC** Fuel Cell
- **FCEV** Fuel Cell Electric Vehicle
- **GC** Glassy Carbon
- **GDL** Gas Diffusion Layer
- **HER** Hydrogen Evolution Reaction
- **HOR** Hydrogen Oxidation Reaction
- **ICE** Internal Combustion Engine
- **MEA** Membrane Electrode Assembly
- **NHE** Normal Hydrogen Electrode
- **NTNU** Norwegian University of Science and Technology
- **ORR** Oxygen Reduction Reaction
- **PEM** Proton Exchange Membrane

- **PEMFC** Proton Exchange Membrane Fuel Cell
- **RE** Reference Electrode
- **RDE** Rotating Disk Electrode
- **rds** Rate-Determining Step
- **rpm** Rotation per Minute
- **S(T)EM** Scanning (Transmission) Electron Microscopy
- **TEM** Transmission Electron Microscopy
- **TPB** Triple Phase Boundary
- **UV-Vis** Ultraviolet-Visible Light
- **WE** Working Electrode
- **XC-72** Vulcan XC-72 Carbon Black
- **XRD** X-ray Diffraction

CHAPTER

ONE

INTRODUCTION

1.1 Background and Motivation

The global demand for hydrogen has increased more than threefold compared to 1975. High-purity hydrogen finds applications in sulfur removal in oil refining and as a precursor gas ammonia synthesis, essential for artificial fertilizers production. While other major chemical processes, such as methanol synthesis and direct reduction of iron, require hydrogen in gas mixtures [1, 2]. Hydrogen is currently produced primarily from fossil sources. Hydrogen derived from natural gas with implemented carbon capture (utilization) and storage
(CC(U)S) is known as *blue hydrogen*. Around three-quarters of the global dedicated hydrogen production is supplied by natural gas using steam methane reforming, and an estimated share of 23% is produced from coal gasification. Only 2% of dedicated hydrogen production is produced by electrolysis [1]. Water electrolysis utilizes electricity to split water into hydrogen and oxygen. Significant carbon footprint reduction can be achieved by water electrolysis powered by electricity from renewable energy sources, termed *green hydrogen* [3]. Although hydrogen production from water electrolysis is generally more costly compared to production by nonrenewable sources, it can be made more cost-effective by increasing production in periods of excess electricity from renewables when the electricity prices are lower [1, 4].

The use of blue and green hydrogen is an option to decarbonize the so-called "hard-to-abate" heavy industry and heavy-duty transport sectors. These sectors are difficult to decarbonize as they require energy inputs that are challenging to achieve by direct electrification by renewable energy sources [5, 6]. Electrification of the transport sector has been on the rise throughout the past decade [7]. Battery electric vehicles (BEVs), using lithium-ion battery technology, currently dominate the light-duty vehicle segment [8]. Fuel cell electric vehicle (FCEV) commercialization and fueling infrastructure are far behind BEV solutions. However, advantages of FCEVs include longer driving ranges and shorter fuelling times compared to BEVs [9]. Further improvements in FCEV technology make them an attractive prospective option for decarbonizing the transport sector [6]. Hydrogen-based energy carriers, as an alternative to fossil fuels, have especially gained traction to achieve decarbonization goals in the heavy-duty transport sector [10].

Hydrogen is proposed as an energy carrier to abate environmental impacts associated with the combustion of fossil fuels. However, the commercialization of proton-exchange membrane (PEM) fuel cells (FC) and water electrolyzer (WE) technologies face challenges related to the substantial cost and reproducible performance of Platinum Group Metals (PGMs) commonly used as an electrocatalyst in such electrochemical devices [9].

Scale-up of fuel cell manufacturing and catalyst production volumes and reducing catalyst loading are considered the most impactful cost-reduction measures for PEM technology solutions [6, 9]. Sonochemical synthesis is a promising method for addressing these issues as it has proven successful in producing electrocatalysts with controlled properties without hazardous reducing agents such as sodium borohydride $NaBH_4$ or contaminating capping agents commonly used in chemical synthesis methods [11]. Sonochemistry concerns the application of "power ultrasound," which is nonlinear low-frequency high-intensity (LFHI) ultrasonic waves (20 kHz - 1 MHz), to generate locally intense temperatures and pressures associated with acoustic cavitation to mediate chemical reactions. Sonochemical synthesis of metal nanoparticles is achieved by reducing metal ions with radicals that are continuously generated by sonolysis of water accompanying acoustic cavitation throughout the reactor [12]. The continuous supply of reducing agents and mixing due to ultrasonic waves promotes homogeneity of the sonochemical reaction environment, which is beneficial for reproducible particle properties [13, 14, 15].

Only a limited amount of work in the literature has been dedicated to scale-up of sonochemical synthesis. Scale-up has mainly been achieved by using multiple parallel reactors [16, 14]. Geometric optimization by increasing the reactor height was studied by Son Y et al. and was suggested to be an important parameter for achieving high sonochemical activity [17]. Asakura and Yasuda investigated the effect of frequency and power for moderately increased reactor volumes by increasing the reactor height and found that larger reactors can provide higher reaction rates by accommodating higher acoustic power and were favorable for avoiding loss of sonochemical activity by bubble coalescence. However, increasing the reactor height will decrease the acoustic pressure as the ultrasonic wave is attenuated by increased interactions with the medium [18, 19].

Metal particle synthesis conditions depend on the amount and distribution of the reducing agent formed. The radical formation depends on the magnitude of acoustic cavitation, meaning the number of cavitation bubbles formed and the energy released during cavitation bubble collapse. Acoustic cavitation is governed by the acoustic field configuration, which depends on the frequency and power specific to the reactor geometry and the fluid medium. While parameters such as fluid temperature, dissolved gas species, and concentration of radical scavengers affect the energy released and radical species formed. Increasing the reactor height will both provide effects that promote and contravenes acoustic cavitation. Successful scale-up of sonochemical synthesis of Pt/XC72 requires that the radical formation is maintained or improved by the combined effects of increasing the reactor height.

1.2 Aim of the Project

This work aimed to scale-up and optimize sonochemical synthesis of Pt/XC72 electrocatalysts with reproducible physical properties and catalytic activity towards the hydrogen evolution reaction (HER) and oxygen reduction reaction (ORR) for fuel cells and electrolyzer applications. The intended outcome is to strengthen hydrogen's position as a fuel by reducing catalyst costs to mitigate environmental impacts associated with the combustion of fossil fuels in the transport sector. The synthesis was performed by reduction of the precursor salt $PtCl_4$ using a 346 kHz ultrasonic plate transducer.

The effects of scale-up of reactor volume on the sonochemical efficiency were characterized by dosimetry and calorimetry, continuing the work conducted during the specialization project in the fall of 2022. Visualization of the sonochemically active regions was performed by sonochemiluminescence.

Optimization of radical scavenger concentration was performed by colorimetry as a preliminary measure for reducing the synthesis time of Pt/XC72. Calorimetry was also used to monitor the reduction of Pt-ions during synthesis, and the effect on synthesis time for syntheses with and without XC72 present from the start. The effect of increased sonication time on particle crystallinity was assessed by XRD. These results were then compared to TEM. Size distribution and phase purity were also investigated by TEM and XRD, and were compared to S(T)EM in combination with EDS.

Physical characterization by BET was used as a complementary method to the hydrogen under deposition and CO-stripping voltammetric methods for Pt surface area measurement. The surface area was used to calculate the current density, without normalizing on catalyst loading determined by TGA, for assessing the catalytic activity towards the HER and ORR.

CHAPTER

TWO

THEORY

2.1 Mitigation of Environmental Impacts in the Transport Sector

Air pollution due to greenhouse gas (GHGs) emissions such as NOx, SO_2, CO, and particulate matter (PM) due to has been shown to negatively impact human health and ecosystems [20, 21]. It is estimated that around 7.98 Gt CO_2 eq. was emitted in the transport sector in 2022, constituting about one-fifth of the global CO_2 emissions considering the sectors "power", "industry", "building", and "transport" [22]. The light-duty vehicles (LDVs) segment was the largest source of direct emissions in the transport sector in 2010 [8].

The known fossil reserves of coal, oil, and gas are expected to last 139, 54, and 49 more years, respectively, based on current production levels [23]. Global efforts are in motion to transition away from fossil fuels and develop alternative fuels [24, 10]. Actions and a suggested timeline for initiating actions to achieve net-zero carbon dioxide emissions into the atmosphere by 2050 were presented in the Net-Zero Emissions by 2050 Scenario (NZE) published by the International Energy Agency in 2021. Increased demand for passenger travel is predicted to be close to double, and fright activity is estimated to increase by 2.5 times from today's levels. Even with increased demand, the NZEs predict that a target value of about 0.7 Gt CO_2 eq. in 2050 could be possible with substantial efforts in technology improvements, renewables, and policy-making [24].

Their primary strategy for decarbonizing the transport sector is implementing technology transitions towards electrification [24]. Currently, battery electric vehicles (BEVs) using Li-ion batteries dominate the electric vehicle segment [8]. However, the International Energy Agency highlights the importance of electrification by using hydrogen as an energy carrier in addition to BEVs for decarbonizing the transport sector [24].

Fuel cell technology has the advantage of much shorter fuelling times, longer driving ranges, and generally lighter weight compared to BEVs, which makes them suited to fulfill the technical requirements of heavier modes of transport, such as shipping, aviation, and long-haul road freight. Increasing the driving range by

battery technology introduces additional weight from the battery pack and other mechanical components, making it more challenging to electrify heavier modes of transport by battery technology. However, battery electric vehicles have experienced much technological maturity over the past decade, and the refueling infrastructure is far ahead of FCEV [5, 9, 7, 24].

Requirements for passenger, cargo, personal vehicles, and other modes of transport vary significantly in terms of intended use, safety, and performance. When comparing BEVs and FCEVs, one should consider the requirements of the intended use and their environmental impact over the entire life cycle of conveyance. The environmental impact throughout the life cycle will be significantly affected by regional differences. Electric vehicles have negligible direct tailpipe emissions when using electricity or hydrogen from renewable energy sources. However, there is a large environmental impact associated with production. Regional differences in the fraction of electricity from fossil fuels in the electricity mix are one of the most important parameters to evaluate for accurately representing emissions over the lifetime of an EV [8].

Scale-up of production and use of hydrogen and hydrogen-based fuels will be essential to reach decarbonization targets of 30 EJ by hydrogen in the 2050 NZE Scenario. There is, however, much uncertainty due to the varying maturity of the different transport technologies. Therefore, the NZE emphasizes the necessity of infrastructure planning and policies that promote investment in supply infrastructure, optimization of passenger transport, and incentivize consumers to adopt more environmentally friendly solutions [24].

2.2 Polymer Electrolyte Membrane Fuel Cell and Water Electrolyzer

Various fuel cell technologies are being investigated for vehicle applications. However, the low-temperature proton exchange membrane fuel cell (PEMFC) is the most promising technology for personal FCEVs. PEMFCs are powered by electricity generated by electrochemical reactions between hydrogen and oxygen. The reactions can be reversed by applying electricity to a proton exchange membrane water electrolyzer (PEMWE) to split water into high-purity hydrogen and oxygen. FCEVs' environmental benefits include practically no tailpipe greenhouse gas (GHG) emission as only water vapor formed during operation. The electrochemical reactions on each electrode are given according to the following half-cell reactions [25, 26]:

Anode: $2\,H_2 \longrightarrow 4\,H^+ + 4\,e^-$ $\qquad E_c^0 = 0$ V

Cathode: $O_2 + 4\,e^- + 4\,H^+ \longrightarrow 2\,H_2O$ $\qquad E_a^0 = 1.229$ V

Overall reaction: $2\,H_2 + O_2 \longrightarrow 2\,H_2O$

The reversible cell voltage, E_{rev} can be found from the Nernst equation 2.1:

$$E_{rev} = E^0 - \frac{RT}{zF} ln \frac{a_{red}}{a_{ox}} \tag{2.1}$$

Where the standard electrode potential with respect to the hydrogen reference electrode is given by E^0, the gas constant is denoted by R, the temperature is given by T, z is the number of electrons partaking in the reaction, the Faraday constant is given by F, and a denotes the activity of the electrochemically active species [27].

Acidic PEMFC and PEMWE own their names for the electrolyte used, a polymer electrolyte membrane (PEM), typically Nafion® , which is selectively permeable to protons and also functions as an electrical insulator. Hydrogen fuel and oxygen are supplied at the anode and cathode end plates, respectively. Platinum group metal (PtGM) nanoparticles loaded on a support material, typically a type of carbon black, make up the catalyst layer and catalyze both the hydrogen and oxygen reactions. Three-phase contact must be established between the catalyst layer, polymer electrolyte membrane (PEM), and the gas diffusion layers (GDLs), which constitute the membrane electrode assembly (MEA), for optimal mass and energy transportation [28, 27].

Hydrogen is split into protons and electrons at the anode. Electroneutrality is maintained as the electrons travel in an outer circuit to the load, and the protons travel through the PEM to the cathode side, where they react with oxygen and form water. The gas diffusion layers are typically made out of carbon cloth or Toray paper. Its porous structure enables fuel and oxidants to pass through it while electrons are collected [28].

The endplates hold the fuel cell stack layers together and are commonly made of stainless steel, graphite, polyvinyl chloride, or polyethylene. Hydrogen and oxygen are distributed to the gas diffusion layers as they are flown through the integrated flow field of the bipolar plates from opposite sides of the fuel cell. The bipolar plates are commonly made of graphite or stainless steel. Other functions of the bipolar plate include collecting the produced current, separating each MEA if the fuel cell stack consists of multiple cells, facilitating the humidification of the gasses, and transporting the produced heat away. Gaskets are placed between the hardware components and the MEA to avoid gas leakage [29, 26].

A schematic drawing of a polymer electrolyte membrane fuel cell components and the catalyst layer on the electrode is shown in Figure 2.2.1.

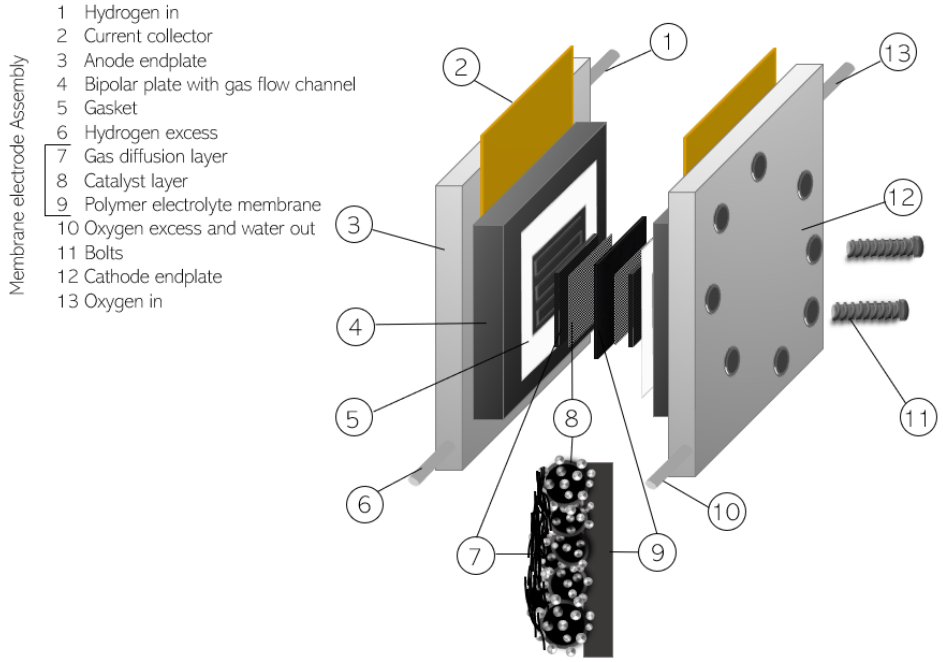

Figure 2.2.1: Schematic diagram of a polymer electrolyte membrane fuel cell. Redrawn with inspiration from [30]. A magnified illustration of the catalyst layer is shown in the excerpt [31].

2.2.1 Voltage Losses in Fuel Cells

The theoretical potential in a PEMFC is 1.229 V at standard conditions assuming no current is drawn. When the potential of an electrode changes as a current is passed through, it is said to become polarized. There are three polarization contributions called ohmic, transport, and kinetic. The additional electrical potential differences to the positive Gibbs energy requirement of the cell are called the overvoltage [32].

1) Ohmic polarization

Ohmic polarization occurs due to the slowness of ionic migration and can be observed as a resistance.

2) Transport polarization

Transport polarization originates from diffusion and migration, which cause slowness in the supply and removal of reactants and products, respectively.
3) Kinetic polarization
Kinetic polarization is due to the inherent speed of electrode reactions.

The operating potential of the fuel cell is lower than the ideal potential due to the

voltage drop caused by polarization, as shown in equation 2.2 [27, 32].

$$E_{\text{cell}}(i) = E_{\text{rev}} - (|\eta_{\text{a}}| + \eta_{\text{c}} + iR_{\text{Ohmic}}) \tag{2.2}$$

, where E_{rev} is the reversible open circuit potential of the fuel cell given by equation2.1, i is the current density, R_{Ohmic}) is the ohmic resistance, η_{a} and η_{c} are the anodic and cathodic overpotentials, respectively.

A typical polarization curve showing the potential dependence of the current density of a fuel cell described by equation 2.2 is shown in Figure 2.2.2.

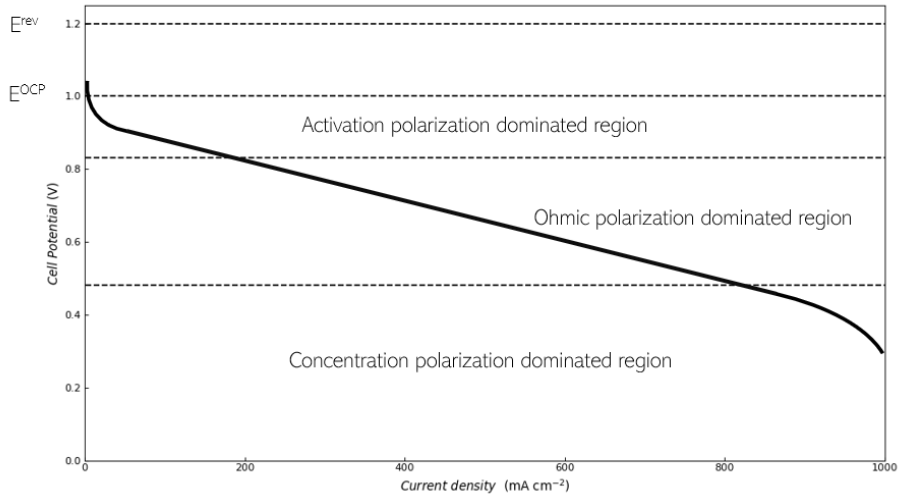

Figure 2.2.2: A typical fuel cell polarization curve showing different regions where the various polarization contributions affect the observed potential as a function of the current density. Redrawn with inspiration from [28].

The polarization curve can be divided into three regions where the different mechanisms of polarization losses dominate. Corresponding to kinetic polarization, ohmic polarization, and transport polarization, respectively.

The kinetic polarization is often called activation loss, which is shown in region I in Figure 2.2.2. The HER and ORR are the electrochemical reactions taking place at the catalyst surface. Activation losses due to the ORR are greater than those due to the HER, as the kinetics of the ORR are intrinsically slower.

Ohmic polarization dominates the voltage drop in region II in Figure 2.2.2, and is mostly due to ionic transport resistance through the MEA.

Transport polarization dominates in region III in Figure 2.2.2. The potential is reduced to zero if a sufficiently high current is drawn so that the replenishing of reactants and removal of products is slower than the electrochemical reaction necessary to supply that current [29].

2.2.2 Nanocatalyst for the PEM Fuel Cell and Electrolyzer

The kinetic polarization contribution to the cell voltage can be reduced by utilizing a catalyst. Catalysis is said to be either homogeneous or heterogeneous if the reacting species are of the same or of a different specie than that of the catalyst, respectively. A catalyst reduces the activation energy barrier, which must be overcome for a reaction to occur. Adsorbed molecules are brought in contact at the catalyst surface and form intermediate surface complexes with weaker bonds, making it energetically favorable to react and thereby increasing the reaction kinetics [33].

The adsorption and desorption kinetics impact the overall reaction kinetics of the reaction taking place on an electrocatalyst surface. The affinity of the adsorbed species to the catalyst can be quantified by the heat of adsorption of the reactant. Product formation will be limited if the adsorbate-surface interaction is too weak, resulting in poor adsorption of reactants. However, lack of available catalyst surface for reactants will limit the reaction kinetics if the adsorbate-surface interaction is too strong. The optimum rate of reaction is achieved for adsorbate surface interactions of intermediate strength. This is known as Sabatiers principle [34]. A comparison of different metal catalysts shows that the heat of adsorption hydrogen and oxygen is favorable for high reaction kinetics for the platinum group metals. However, the high cost of PtGM is a significant bottleneck for making PEMFC cost competitive with other types of vehicles [9].

A suggested reaction mechanism for the hydrogen oxidation reaction (HOR) is as follows.

$$H_2 \longrightarrow H\cdot + H\cdot$$

$$H\cdot \longrightarrow H^+ + e^-$$

The first step of the HOR is dissociative chemisorption of hydrogen, while the second step involves charge transfer. The overall reaction rate will therefore depend on the number of vacant sites on the electrode surface.

The ORR reaction mechanism is more complicated than the HOR in which both an associative and dissociative mechanism is possible. Steady-state surface adsorption of molecular O_2 is the first step of the reaction and can be considered a chemical step in which a neutral species is adsorbed [35].

Associative ORR reaction mechanism

$$O_2 + 4\,H+ + 4\,e\text{-} \longrightarrow OOH\,(ads) + 3\,H+ + 3\,e\text{-}$$

$$OOH\,(ads) + 3\,H+ + 3\,e\text{-} \longrightarrow O\,(ads) + 2\,H+ + 2\,e\text{-}$$

$$OH\,(ads) + H+ + e\text{-} \longrightarrow 2\,H_2O$$

Dissociative ORR reaction mechanism

$$\tfrac{1}{2}\,O_2 + 2\,H+ + 2\,e- \longrightarrow O\,(ads) + 2\,H+ + 2\,e-$$

$$O\,(ads) + 2\,H+ + 2\,e- \longrightarrow OH\,(ads) + H+ + 2\,e-$$

$$OH\,(ads) + H+ + e- \longrightarrow 2\,H_2O$$

The kinetics of the hydrogen oxidation at the anode is much faster than the kinetics of the oxygen reduction at the cathode. Therefore higher catalyst loading is required at the cathode compared to the anode. It is desirable to reduce the use of PtGM catalyst both from an environmental and cost perspective. PtGM nanocatalysts supported on carbon black are commonly used to minimize mineral use while simultaneously increasing the accessible surface for electrochemical reactions, as they have a considerable surface area-to-volume ratio [36]. Around 90% of the atoms in spherical particles around 1 nm, are surface atoms [37].

The current density measured in amps in a fuel cell per unit mass of platinum measured per gram of platinum ($A/g_{Pt}cm^2$) is the mass activity. Mass activity quantifies the higher reaction rate due to more available surface area. A common platinum loading for the cathode used in research is $0.3\,mgPt/cm^2$, whereas long-term target loadings are in the range of $0.0625\,mg_{Pt}/cm^2$ [36].

Enhancing the electrocatalyst performance and properties is essential for improving fuel cell efficiency, increasing the lifetime with reproducible performance, and lowering the initial cost. The lifetime of the catalyst is dependent on the stability of the supported PtGM. Reliable, reproducible performance during operation is necessary for the commercialization of PEMFC. Diminished performance is caused by certain operating conditions, such as potential cycling, which cause catalyst layer degradation by platinum dissolution and corrosion of carbon, resulting in a smaller electrochemical surface area (ECSA). Loss of ECSA can also be due to migration and coalescence of Pt-NPs [38]. Careful control of particle properties by tailoring synthesis conditions is required to achieve the optimal Pt particle size of about 3-4 nm for stability and performance in fuel cell applications [36, 39]. However, costs associated with additional time spent on synthesis, complex processing steps, and scale-up limitations of alternative nanocatalyst production may counteract the cost benefits of decreasing the platinum loading [36].

2.3 Electrochemical Characterization of Catalyst Properties

The properties and performance of electrocatalysts can be investigated by electrochemical characterization ex-situ, typically in an electrochemical cell with a three-electrode setup or in-situ in their intended application. Voltammetry is a collective term for electrochemical techniques in which the measured current response is presented as a function of applied potential. Voltammetric techniques are commonly applied to study electrocatalysts [39].

2.3.1 The Three Electrode Setup

The three-electrode setup is used to study electrochemical processes ex-situ. The setup consists of a working electrode (WE), a counter electrode (CE), and a reference electrode (RE). Processes of interest, such as electrochemical reactions, take place at the WE. A CE is coupled to the WE to enable current flow by completing the circuit. The potential of the working electrode is measured with respect to a RE, and controlled by a potentiostat. The potentiostat is also used to record the current from the CE [32].

2.3.2 Linear Sweep Voltammetry

Linear sweep voltammetry (LSV) is an electrochemical technique commonly used to investigate redox reactions and thereby finds applications in assessing electrocatalyst activity. In LSV, the current response in the WE that originates from the potential between the WE and RE is recorded. The potential is swept linearly in time in either the anodic or cathodic direction, is measured [39].

The potential for an oxidation or reduction reaction for a given time as a function of an either positive or negative potential sweep, respectively, is given by equation 2.3.

$$E_{\mathrm{t}} = E_{\mathrm{i}} \pm \nu t \tag{2.3}$$

Where E_0, is the initial potential which is set to a value with negligible current flow. The sweep rate is given by ν, and t denotes the time [39].

As the potential changes, the current will increase in magnitude as a response to the accompanying change in the concentration of reactants and products near the electrode surface. The current will reach a vertex point when the thickness of the diffusion layer has grown to the extent where the supply of reactant becomes diffusion limited, causing the current to taper off. Slower scan rates enable the diffusion layer to grow thicker compared to faster scan rates. If the sweep rate is sufficiently low, the concentration gradients can attain minimal values and be stationary, whereby the LSV is said to be quasi-stationary [39].

Polarization curved from linear sweep voltammetry is commonly used to assess electrocatalyst performance. Although Pt has high activity toward the HER reaction, it has been reported in the literature to exhibit varied electrocatalytic performance. This has been attributed to variations in the experimental parameters used and incongruence in performance evaluation methods, such as using different methods to normalize the current density. Objective comparison between catalyst activities can therefore be difficult. The overpotential needed to reach -10 mAcm^{-2} is a common benchmark value for the HER reaction [40], while a common benchmark value for ORR activity is the current density at 0.9 V vs. (RHE)[41]. Factors such as the electrolyte temperature and resistance (R_s), charge transfer resistance (R_{ct}), Pt loading, and particle microstructure have been shown to affect the performance of platinum catalysts[40].

2.3.3 Electrochemical Impedance Spectroscopy

Electrochemical impedance spectroscopy (EIS) is a method commonly used to determine the resistances in an electrochemical system by relating the system's

impedance to measured time-dependent current from the time-dependent potential. Instead of recording the current as a function of potential, as for the voltammetric methods, the current response is recorded as a function of frequency. An AC current will be generated by applying an AC voltage, usually providing a sinusoidal potential excitation. The current response can be treated as a Fourier series [42, 34].

The time-dependent excitation signal can be expressed as shown in equation 2.4

$$E_{\mathrm{t}} = E_0 sin(\omega t) \tag{2.4}$$

, where the signal amplitude is given by E_0. The radial frequency is denoted ω denoted which can be written as equation $\omega = 2\pi$ f (rad s^{-1}).

For a linear system (i.e., that superposition is valid), the time-dependent response signal can be expressed as equation 2.5

$$I_{\mathrm{t}} = I_0 sin(\omega t + \phi) \tag{2.5}$$

, in which the response signal I_0 has undergone a phase shift (ϕ) and attained another amplitude than I_0.

The impedance of the system can then be described as shown in equation 2.6

$$Z = \frac{E_{\mathrm{t}}}{I_{\mathrm{t}}} = \frac{E_0 sin(\omega t)}{I_0 sin(\omega t + \phi)} = Z_0 \frac{sin(\omega t)}{sin(\omega t + \phi)} \tag{2.6}$$

The impedance can be expressed as a complex function as shown in equation 2.10, by reformulating equation 2.4 and equation 2.5 using the Euler identity shown in equation 2.7

$$exp(j\phi) = cos(\phi) + jsin(\phi) \tag{2.7}$$

The reformulated excitation and response signals are presented in equations 2.8 and 2.9, respectively.

$$E_{\mathrm{t}} = E_0 exp(j\omega t) \tag{2.8}$$

$$I_{\mathrm{t}} = I_0 exp(j\omega t - \phi) \tag{2.9}$$

$$Z(\omega) = \frac{E}{I} = Z_0 exp(j\phi) = Z_0(cos(\phi) + jsin(\phi)) \tag{2.10}$$

A graphical representation of the impedance as a complex function with the real and imaginary parts plotted on the x-axis and y-axis, respectively, is called a *Nyquist Plot*. For an electrochemical system where the impedance is dominated by electron-transfer resistance the Nyquist plot can be represented as shown in Figure 2.3.1.

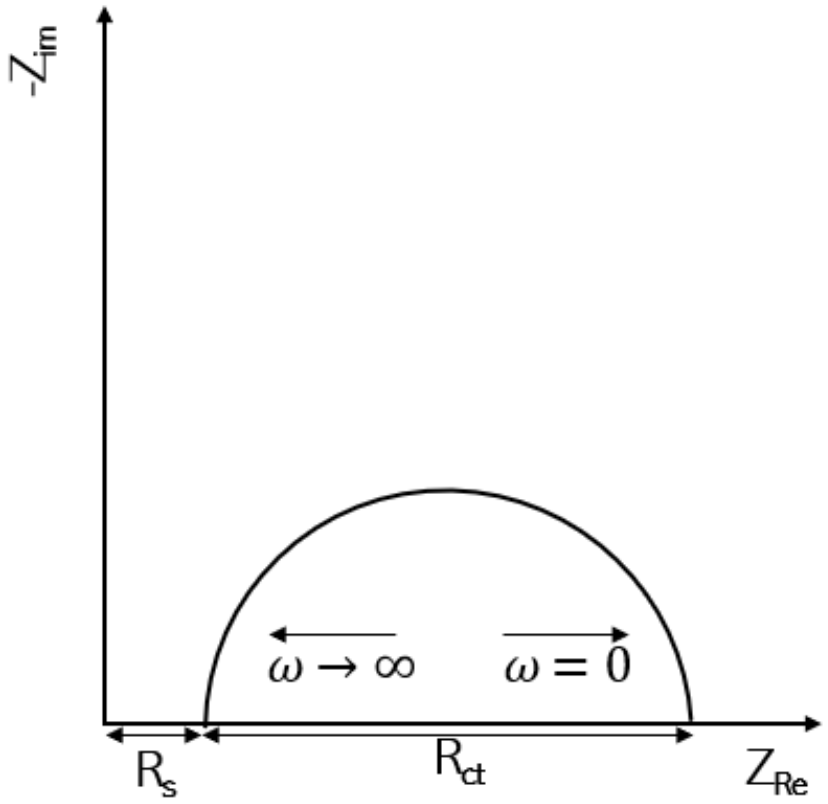

Figure 2.3.1: Nyquist plot for an electrochemical system where the impedance is dominated by electron-transfer resistance. Redrawn with inspiration from [34].

The solution resistance (R_s) and the charge transfer resistance (R_{ct}) can be found at the high frequency and lower frequency intercept with the x-axis, respectively. The iR-drop caused by ohmic resistance can be corrected by using R_s.

2.3.4 Cyclic Voltammetry

Cyclic voltammetry (CV) is arguably the most commonly used electrochemical technique to study electrode films and processes. Its versatile applications can be used to characterize surface reactions and processes, such as reaction mechanisms, determining the electrochemically active surface area, the effect of contaminants, alterations in surface activity, which potential ranges different reactions occur, and kinetic parameters. Similar to LSV, the current response is recorded as the potential is swept in either anodic or cathodic directions. However, as the name entails, the potential is cycled between predefined negative and positive switching potentials [34]. Redox-active species are being reduced for negative sweeps yielding a cathodic current (I_{pc}). Oppositely redox-active species are oxidized during positive sweeps resulting in an anodic current (I_{pa}) response. The anodic and cathodic potentials where the sweep direction is reversed, called the switching potential, are chosen where the oxidation and reduction of redox-active species on the electrode surface is complete [43].

The current discussion will revolve around Pt in 0.5 M H_2SO_4. In this system, the switching potentials are predefined to be located between the hydrogen and oxygen evolution potentials in aqueous solutions. Adsorbed impurities may obscure the electrode process of concern. The switching potentials should be high enough to remove impurities by reduction and oxidation. Chemisorbed oxide and hydride layers are formed and dissolved on the electrode surface during a cycle for an aqueous solution with no redox-active couples. The HER occurs thermodynamically at 0 V for the Pt in 0.5 M H_2SO_4 system, with an RHE as the reference electrode. From anodic sweeps between about 450 mV to 550 mV, a capacitive current response is associated with the charging of the electrolytic double layer (i_c). The capacitance electrolytic double layer is C_d. The charging current is related to the capacitance and change in potential through the relation $i_c = C_d \cdot dE/dt$ for which $\nu = dE/dt$. The hydroxide discharge process initiates the chemisorption of oxygen for potentials above 550 mV, as shown in the following reaction equation [34].

$$Pt + OH^- \longrightarrow Pt\text{-}OH + e^-$$

Additional oxidation occurs when the advancing to potentials higher than about 800 mV, as shown in the following reaction equation

$$Pt - OH + OH^- \longrightarrow Pt\text{-}O + H_2O + e^-$$

The OER occurs above around 1600 mV, and formation of a phase oxide may be formed on the electrode surface. Oxygen gas in the near vicinity of the electrode is reduced alongside the chemisorbed oxide layer when the direction of the potential sweep is reversed. A new double-layer region appears with subsequent hydride deposition when sweeping to lower potentials, as shown in the following reaction equation

$$Pt + H_2O + e^- \longrightarrow Pt\text{-}H + OH^-$$

The HER takes place when the potential sweep approaches 0 V. Re-oxidation of hydrogen occurs when the potential sweep is switched back to the anodic direction [34].

The various regions for the different reactions and surface processes are illustrated in Figure 2.3.2

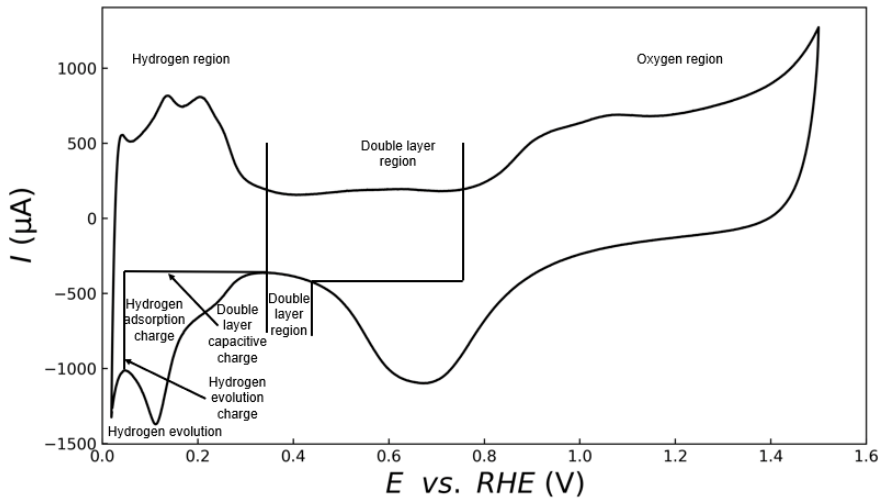

Figure 2.3.2: Cyclic voltammogram of Pt/XC72 in 0.5 M H_2SO_4 solution bubbled with Ar, with the hydrogen, double layer, and oxygen region indicated. A scan rate was $\nu = 50$ mV s^{-1}. The illustration was redrawn from [44, 34] in and used in the specialization project [31].

The differential capacitance C_d is associated with film formation at equilibrium coverage. C_d is defined as *the rate of increase of charge with potential* mathematically expressed as $C_d = dQ/dE = i/(dE/dt) \equiv i/\nu$, under the assumption that the film coverage occurs faster than the sweep rate [34]. The recorded current evolved by forming or removing a complete film layer can be integrated to find the charge associated with this prosses as shown in equation 2.11

$$Q_F = \int idt = \int dQ(E) = \int C^d(E)dE \tag{2.11}$$

This charge can be used to find the electrochemical surface area (ECSA), which can be used as a measure of the real Pt surface area [34]. Accurate measurements of real surface area are essential to ascertain information about the specific catalyst activity as it relates the observed currents to the per-site turnover [45]. Integration of the charge produced by desorption of a underpotentially-deposited hydrogen adlayer H (H_{UPD}) ($H_{UPD}(ads) \longrightarrow H^+ + e^-$) is called the hydrogen under potential deposition (H_{UPD}) method for determining ECSA [41]. A monolayer of H adsorbed onto Pt surface atoms corresponds to a charge of $220\,\mu C\,cm^{-2}$ [46].

Another way to measure ECSA is by the CO-stripping voltammetry method, in which CO that has been pre-adsorbed on Pt is electrochemically oxidized [47]. CO is a catalytic poison for Pt as it requires rather high potentials of about 0.6 V and higher vs. RHE to attain appreciable rates of CO oxidation, and thereby block active sites on the catalyst surface. The poisoning is thought to be due to the combination of fairly high enthalpy of adsorption of CO on Pt and the limitations introduced by the reaction mechanism. The oxidation of CO to CO_2 is thought to follow a Langmuir-Hinshelwood reaction mechanism as it involves a surface reaction of adsorbed CO and an adsorbed oxygen-containing molecule [47].

A simplified form of the reaction mechanism is presented below.

$$H_2O + Pt \longrightarrow OH\,(ads) + H^+ + e^-$$

$$CO\,(ads) + OH\,(ads) \longrightarrow CO_2 + H^+ + e^- + 2\,Pt$$

An underlying assumption of the Langmuir-Hinshelwood mechanism is that the surface reaction is the rate-determining step, meaning that the rate will be dependent on the surface coverage of both species for such a bimolecular reaction [47]. Linearly, bridge-bonded, and multiply bonding configurations CO can occur on Pt, some studies have suggested that reducing the particle size below 5 nm will promote linearly bound CO [37]. A charge of $420\,\mu C\,cm^{-2}$ is evolved by the oxidation of CO [47].

2.3.5 Cyclic Volmtametry in Presence of Oxygen in the Electrolyte

Current contributions from film formation to the are overlaid with the current contributions from the electrode reactions if the electrolyte is bubbled with an electrochemically active species such as O_2. Quasi-stationary current contributions from the ORR are attained as current contributions from film formation on Pt become negligible when O_2 is present in the electrolyte [34].

2.4 Fundamental Aspects of Ultrasonics and Application of Sonochemistry

Sonochemistry is the application of "power ultrasound", which is low-frequency high-intensity (LFHI) ultrasound, to mediate chemical reactions. LFHI are mechanical vibrations ranging from 20 kHz - 1 MHz with high sound intensity power, ranging from 10 - 1000 W/cm^2, from which power ultrasound owes its name [48, 49]. LFHI ultrasound adheres to the nonlinear acoustic regime. Acoustic cavitation is a phenomenon caused by the high energy density released by the implosion of cavitation bubbles induced by nonlinear acoustics. Acoustic emissions from cavitation include phenomena such as the generation of high temperatures, plasma formation, light emission (sonoluminescence), formation of high-speed liquid jets, shock waves, and sound emission [50]. The high temperatures generated by acoustic cavitation can be utilized to generate radicals as a reducing species for metal ions in metal nanoparticle synthesis [12]. Enhancement of sonochemical reactions can be achieved by careful control of the ultrasonic field. Optimal scale-up design of sonochemical systems, therefore, necessitates insights into the physical properties of ultrasound [51]. The fundamental aspects of ultrasonics and the application of sonochemistry for producing nanoparticles are presented in the following subsections.

2.4.1 Generation of Power Ultrasound by Transducer Plate and Scale-Up Limitations

Ultrasonic waves are generated by a transducer, which typically consists of a ferroelectric ceramic such as lead zirconate titanate (PZT) [12]. Ferroelectric materials exhibit spontaneous polarization, meaning they are polar without the influence of an electric field. The converse piezoelectric effect is a piezoelectric property of the ferroelectric crystal that makes it possible to transform electric energy into mechanical vibrations [48, 52].

Various transducer geometries exist and can be divided into variations of the two geometries, *ultrasonic horns* and *plate transducers*. Only plate transducers will be discussed for nanoparticle synthesis applications. An ultrasonic plate transducer typically consists of a (PZT) crystal mounted between metal plates. The transducer generates ultrasonic waves by the displacement of fluid caused by the motion component normal to the mechanically vibrating surface. The fluid motion causes a response in pressure whereby the periodic expansion and contraction cause a decrease and increase in pressure, respectively. The sound waves propagate by the periodic transient pressure change, which causes fluid molecules adjacent to one another to be set in motion [51]. Generation of ultrasound is achieved by tuning the transducer unit frequency to half-wavelength of the operating frequency. Causing the transducer plate to vibrate with relatively large displacements compared to its own dimensions [53].

Constraints associated with the achievable transducer size, power, and capacity pose scale-up limitations of sonochemical reactors. Transducer performance is affected by nonlinear phenomena, which are yet not fully understood, such as modal interactions and frequency shifts when they are operated at high powers.

Mechanical limitations include material fatigue and elastic nonlinearities, which become prominent when the transducer is driven with high amplitudes. Thermal limitations include the depolarization of piezoelectric ceramics when subjected to a significant temperature increase [53].

As of today, ultrasonic devices are predominantly mounted in parallel lines to achieve industrial-scale applicability. The radiating plate has the greatest impact on the radiation field configuration, efficiency, and power capacity. The need for dedicated studies on optimizing the geometrical configurations of the tuned components, the location and distribution of thermal stresses, mechanical stresses, and the fatigue limitations of the materials of transducers operated at high power are recognized as one of the barriers to optimizing scale up of sonochemical reactors. System design by finite element modeling (FEM) has attracted interest for its versatility and applicability for the optimization of new ultrasonic power generators by providing analytical transducer design, the meshing of the geometry of the transducer by 3D modeling, static analysis of stresses, and modeling of the acoustic field by analysis of the modal, dynamic and acoustic–structure interaction [53].

2.4.2 Fundamentals Ultrasonic Waves

Initially, ultrasonic waves propagating through a fluid have a sinusoidal form. Propagation of the ultrasonic waves with low intensity can be described by a set of linearized hydrodynamic equations (2.12 and 2.13) describing the conservation of momentum and mass, the entropy equation, and the equation of state. Some of the energy of the propagating ultrasonic wave is transformed into thermal energy due to interactions with the fluid due to its thermal conductivity and viscosity, causing wave absorption. The hydrodynamic equation must include these contributions to account for wave absorption [19, 54].

$$\rho\left[\frac{\partial \mathbf{v}}{\partial t} + (\mathbf{v}\cdot\nabla)\mathbf{v}\right] = -\nabla p + \eta\nabla v + (\zeta + \frac{\eta}{3})\nabla(\nabla\cdot v) \tag{2.12}$$

The conservation of mass is given by equation 2.13.

$$\frac{\partial \rho}{\partial t} + \nabla\cdot(\rho\mathbf{v}) = 0 \tag{2.13}$$

The heat transfer is described by the entropy equation 2.14.

$$pT\left[\frac{\partial s}{\partial t} + (\mathbf{v}\cdot\nabla)s\right] = \kappa\nabla T\frac{\eta}{2}\left(\frac{\partial v_i}{\partial x_j} + \frac{\partial v_i}{\partial x_i} - \frac{2}{3}\delta_{ij}\nabla\cdot\mathbf{v}\right)^2 + \zeta(\nabla\cdot\mathbf{v})^2 \tag{2.14}$$

The equation of state is presented in equation 2.15

$$p = p(\rho, s) \tag{2.15}$$

The density is given by ρ, the particle velocity is given by the vector $\mathbf{v} = (v_x, v_y, v_z)$, the pressure is denoted by p, the temperature is given by T, s denotes the entropy, δ_{ij} is the Kronecker delta, shear viscosity is given by η, bulk viscosity is given by ζ, and the thermal conductivity is given by κ. The latter three variables are

assumed to be constants [54, 19].

The thermodynamic variables ρ_0, p_0, T_0 and s_0 characterizes the liquid when it is not moving ($\mathbf{v} = 0$). When the liquid is set in motion, it is characterized by the perturbations of velocity $\mathbf{v}$, density ρ' = ρ - ρ_0, pressure p' = p - p_0, temperature T' = T - T_0, and entropy s' = s - s_0. The decomposition of each perturbation yields three independent modes of fluid behavior, which are the acoustic, vorticity, and entropy mode [19].

The vorticity mode only influences the velocity of the fluid. Fluid behavior related to heat transfer phenomena is described by the entropy mode. The entropy mode perturbs all thermodynamic parameters, but the effect on pressure is negligible [19].

The acoustic mode perturbs all the thermodynamic parameters when it is excited. The wave equation that describes acoustic pressure is given by equation 2.16

$$\frac{\partial^2 p_{\mathrm{aq}}}{\partial t^2} - c_0^2 \nabla_{\mathrm{ac}} \approx \delta \frac{\partial}{\partial t} \nabla p_{\mathrm{aq}} \tag{2.16}$$

, where the speed of sound in an unagitated system is given by c_0^2 and the diffusivity of sound is given by the following term $\delta = [4\eta/3 + \zeta + \kappa(c_{\mathrm{v}}^{-1} - c_{\mathrm{p}}^{-1})]/\rho_0$ in which c_{v} and c_{p} are the specific heat at constant volume and pressure, respectively [19]. By disregarding the thermal conductivity and viscosity, assuming no entropy perturbations and that the temperature and density perturbations are adiabatic, then equation 2.16 becomes the classical wave equation describing the propagation of ultrasonic waves with a sound velocity c_0.

$$\rho_0 = \left(\frac{\partial u}{\partial t} + u \frac{\partial u}{\partial x} \right) = \frac{\partial u}{\partial x} \tag{2.17}$$

By assuming u $\approx$ 0 then equation 2.17 can approximated by equation 2.18

$$\rho_0 \frac{\partial u}{\partial t} = -\frac{\partial p}{\partial x} \tag{2.18}$$

The equation of state 2.15 can be expressed as the ratio of change in density

$$p = K \frac{\rho}{\rho_0} \tag{2.19}$$

, where K denotes the volume elasticity.

The one-dimensional wave equation describing the sound pressure influence of the sound speed can be expressed as equation 2.20, by combining equations 2.18, 2.13 and 2.19.

$$\frac{\partial^2 p_{\mathrm{aq}}}{\partial x^2} - \frac{1}{c_0^2} \frac{\partial^2 p_{\mathrm{aq}}}{\partial t^2} p_{\mathrm{aq}} = 0 \tag{2.20}$$

In which c_0^2 is given by equation 2.21

$$c_0^2 = \frac{K}{\rho_0} \left(= \frac{\partial p}{\partial \rho} \right) \tag{2.21}$$

It follows from the solution of the wave equation 2.20 that the acoustic pressure p exerted on a fluid particle causes it to attain a velocity of u = p/$\rho_0 c_0$ [51]. A fluid particle in a volume will also experience hydrostatic pressure pushing down in the z-direction [54].

The instantaneous power per unit area is the work being applied to a fluid by an ultrasonic wave per unit time and can be expressed as $pu = p^2/\rho_0 c_0$. It follows then that the acoustic power (W/m^2) of an ultrasonic wave can be expressed equation 2.22 [51].

$$I = \frac{|P|^2}{2\rho_0 c_0} \tag{2.22}$$

2.4.3 Nonlinear Phenomena of High-Intensity Ultasound

Perturbations become significant for high-intensity ultrasonic waves. As a consequence, the assumptions of linear acoustics no longer hold, and one enters the nonlinear acoustic regime. Additional sound–vorticity, sound–entropy, and sound-sound interactions between the modes of fluid behavior must be accounted for in addition to the modes themselves when describing an arbitrary flow field in the nonlinear acoustic regime. Nonlinear processes such as harmonic generation, self-demodulation, and acoustic mode waveform distortion occur due to the acoustic mode of fluid behavior. The interactions of the acoustic mode with the vorticity and entropy mode cause other nonlinear processes, such as the generation of hydrodynamic flows and acoustically induced heating, respectively [19]. These phenomena influence the absorption and the pattern of ultrasonic wave propagation greatly [19].

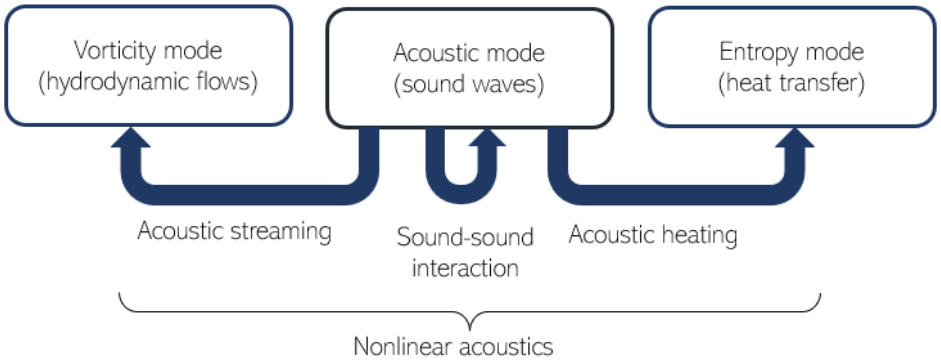

Figure 2.4.1: Phenomena generated by strong perturbations of the different modes of fluid motion in nonlinear acoustics. Redrawn with inspiration from [19]

In linear acoustic, the speed of sound is given by c_0, whereas in nonlinear acoustics, it is given by c + u. There are two contributions to the nonlinear speed of sound, one being the change c_0 into c of the local sound velocity due to nonlinearity in the relation between pressure and density, and the other is medium drift with velocity u [19]. Taylor expansion can be used to include the elastic nonlinearity, introduced from the considerable changes in ρ for an ultrasonic wave with a large amplitude propagating in the x-direction, in the equation of state 2.19, which then can be expressed as 2.23 [51].

$$p = A\frac{\rho}{\rho_0} + \frac{B}{2}\left(\frac{\rho}{\rho_0}\right)^2 \tag{2.23}$$

The equation 2.17 can be written as equation 2.24, by accounting for the additional speed contributions p = $\rho_0 cu$ in a nonlinear regime.

$$\left[\frac{\partial}{\partial t} + (c+u)\frac{\partial}{\partial x}\right] u = 0 \tag{2.24}$$

The one-dimensional wave equation 2.20 describing the acoustic pressure influence of the sound speed can be expressed as equation 2.25 [51].

$$\frac{\partial^2 p_{aq}}{\partial x^2} - \frac{1}{c_0^2}\frac{\partial^2 p_{aq}}{\partial t^2} = -\frac{\beta}{\rho_0 c_0^4}\frac{\partial^2 p_{aq}^2}{\partial t^2} \tag{2.25}$$

Initially, the ultrasonic waves propagate as a traveling wave with a sinusoidal form near the transducer. The wave profile becomes distorted due to locally different velocities of sound, which changes from c_0 to c when transitioning from linear to nonlinear acoustic regime. Fluid molecules in the compressed parts of the wave profile move faster compared to the molecules in refracted portions where the density is smaller. This causes the wavefronts to become increasingly steep, leading to a discontinuity in each period, and as a consequence, the wave profile attains a sawtooth form. The increase in steepness is counteracted by wave absorption due to dissipative processes originating from the influence of thermal conductivity and viscosity, which smoothens the sawtooth profile to attain a sinusoidal form again. Ultrasonic wave absorption exhibits a distance dependency, first increasing with propagation length and then decreasing due to attenuation of nonlinear effects caused by wave amplitude dampening [54]. The traveling ultrasonic wave is reflected due to the density difference at the interface between the liquid medium and the air or a reflector. A standing wave is formed by interference of the forward and backward propagating traveling wave [55]. The sound pressure attains its lowest (zero) at the nodal and maximum values and anti-nodal planes of the standing wave [52]. However, wave attenuation causes the actual sound field to have a standing wave component close to the interface and traveling wave components near the transducer [55]. The ultrasonic propagation and interactions with the medium and surroundings are illustrated in Figure 2.4.2.

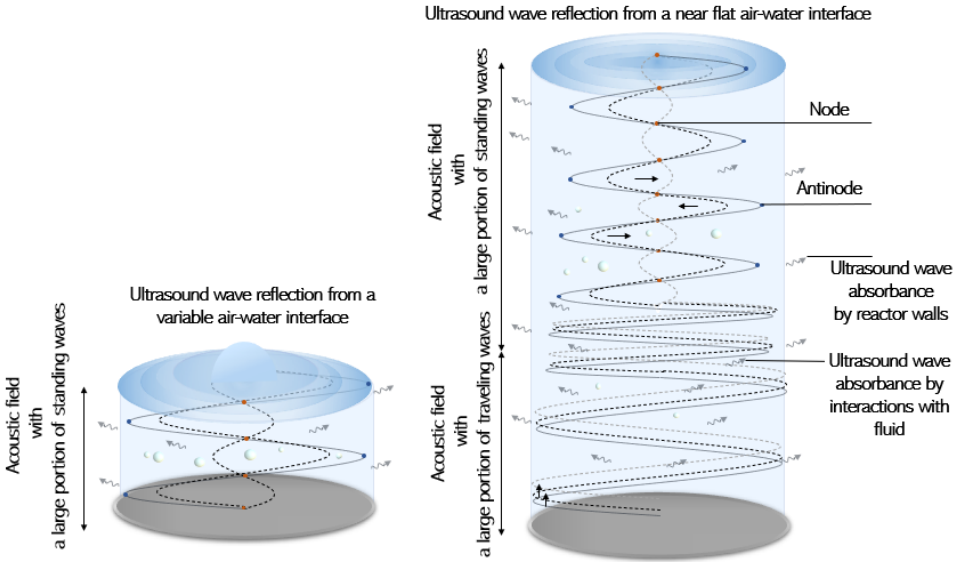

Figure 2.4.2: Illustration of the different ultrasonic wave propagation and interactions for shorter and longer ultrasonic propagation lengths, respectively. The illustration is not to scale.

2.5 Acoustic Cavitation

Acoustic cavitation is a hypernym for the chemical and physical processes associated with the formation, growth, and implosion of cavitation bubbles generated by intense ultrasonic waves [50]. Acoustic cavitation is initiated by bubble nucleation. Bubble nucleation occurs when the liquid ruptures and a cavity forms due to negative pressure from the LFHI ultrasonic wave exceeding the liquid's tensile strength [50]. Ultrasound waves propagate through a liquid medium with a near sinusoidal form, alternating between cycles of compression at wave peaks and rarefaction between peaks. Liquid molecules are brought closer during the compression cycles as the exerted pressure is positive. Oppositely negative pressures are exerted during the rarefaction cycles and consequently separate the molecules [19]. The negative pressure from LFHI ultrasound is not strong enough to split water by overcoming the tensile strength by itself. However, cavitation still occurs due to heterogeneities such as dissolved gas bubbles or gas in crevices of solid impurities, similar to a crack in a solid, which locally reduces the integrity of the medium [56, 50]. The highest negative pressures are attained in the refractive cycle of a standing wave oscillating in an anti-nodal plane [52].

Some bubbles will oscillate weakly and will not contribute to the sonochemical activity. While bubbles with high-energy collapse are called *active bubbles*, as they contribute to sonochemical reactions. The active bubbles can be divided into two groups *fragmentary transient cavitation* or *repetitive transient cavitation (high-energy stable cavitation)*. Fragmentary transient cavitation describes high-energy collapse that causes bubble fragmentation, thereby proliferating new cavitation bubble nuclei. While repetitive transient cavitation is the growth and high-energy collapse of the same bubble multiple times [57]. Cavitation bubbles will be subjected to an acoustic radiation force called the primary Bjerknes force. The primary Bjerknes force directs cavitation bubbles larger than the resonant size toward the sound pressure node or toward the antinode if the bubble size is smaller than the resonant size under standing wave conditions. Another acoustic radiation force called the secondary Bjerknes force originates from the sound waves emitted by the bubbles. The bubbles will be attracted to one another if both bubbles are smaller or larger compared to the resonant size, whereas they will be repelled if one bubble is smaller and the other larger than the resonant size [52]. The secondary Bjerknes force subjected on bubble two by bubble one, with a distance, d, in between them can be expressed as equation 2.26

$$F_{12} = \frac{\rho}{4\pi d^2} V_1 \frac{d^2 V_1}{dt^2} \tag{2.26}$$

, where V_1 is the volume of bubble one and ρ is the liquid density [58].

With an understanding of the acoustic field from section 2.4.3 and the, forces acting upon a cavitation bubble one could try to balance these in a way that would favor acoustic cavitation. The forces acting upon a cavitation bubble are illustrated in Figure 2.5.1, however, their magnitude is not drawn to scale and will be system specific.

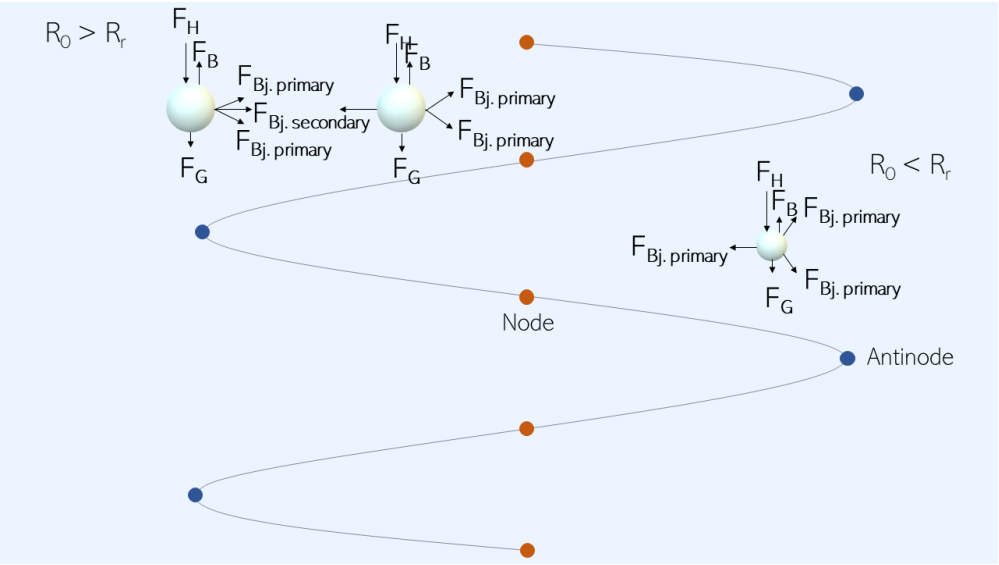

Figure 2.5.1: Illustration of the forces acting upon cavitation bubbles under various conditions in a standing wave field.

Increasing the height increases the hydrostatic pressure, pushing bubbles downwards. Increasing the frequency a higher number of cavitation bubbles and smaller bubbles. The buoyancy force driving the bubbles upwards increased with increased bubble size.

Bubbles that oscillate through many acoustic cycles can grow through a process called rectified diffusion. Cavitation bubbles can also grow by bubble coalescence [57]. Rectified diffusion is growth by an average mass flow into the cavitation bubble due to two different diffusion contributions. The first contribution is termed the "area effect", in which the diffusion of vapor molecules and evaporated gas from bulk solution into the cavitation bubble is promoted by the low internal pressure inside the cavitation bubble during the expansion cycle [12, 52]. The second diffusion contribution is termed the *shell-effect*. A decrease in the gas concentration of the liquid shell surrounding the cavitation bubble accompanies the increase of the shell thickness, which occurs during the compression half cycle. It owes its name to the lower concentration gradient between the dissolved gases in the liquid shell and the bulk, thereby causing fewer molecules to diffuse out of the cavitation bubble. Molecules diffuse into the bubble, which has a lower gas concentration compared to the liquid shell in the subsequent expansion half cycle as the liquid shell has become proportionally thinner compared to the increased bubble size [12, 52]. The increased bubble lifetime during growth by rectified diffusion facilitates the adsorption of surface active solutes, which have been shown to promote the rate of rectified growth and hinder bubble coalescence [59].

The cavitation bubble will continue to grow until it reaches the critical size in

which the cavitation bubble oscillations are resonant with the applied acoustic frequency. This leads to a rapid implosion of the cavitation bubble [12, 60]. The vapors and gasses trapped inside the bubble are heated in a near adiabatic compression during implosion [57]. The temperature and pressures are difficult to measure over the restricted area of the cavitation bubble volume and extremely short collapse durations [60]. The interior of the bubble has been estimated to reach temperatures of 5200 ± 650 K and pressures up to pressures up to 500 atm. The attained temperatures and pressures will be highly system specific [12]. Studies have detected vibronic temperatures of intrabubble plasma for Ar-saturated water with an ultrasonic frequency of 362 kHz were estimated to be T_e = 10000 K and T_ν = 8450 K attained by spectroscopic measurements of light emitted by sonoluminescence during cavitation bubble implosion in Ar-saturated water. These experimental observations and theoretical models of cavitation cannot be explained solely by adiabatic heating but have been attributed to the formation of nonthermal plasma. The chemical reactivity is thought to be increased by the excitation of nonvolatile species in the plasma environment[61].

The following three regions describe the reaction environment created by an imploding cavitation bubble [12].

I) Gas-phase zone
The interior of the collapsing cavitation bubble is a gas-phase zone as it contains gas molecules and volatile solutes accumulated during cavitation bubble growth. Maximum temperature occurs in the gas-phase zone. The extreme reaction conditions cause radicals to be formed by the sonolysis of gaseous species trapped inside the cavitation bubbles. Primary radicals have a short lifetime.

II) Microbubble shell

The microbubble shell is an interfacial region that can attain temperatures of about 2000 K.

III) Bulk solution
Non surface active species reside in the bulk solution. Transport of surface active molecules to the cavitation bubbles is mediated by the bulk solution, as is the transport of the radicals formed by acoustic cavitation out of the cavitation bubble, which then may react with solutes [12].

The three aforementioned reaction environment regions are illustrated in Figure 2.5.2.

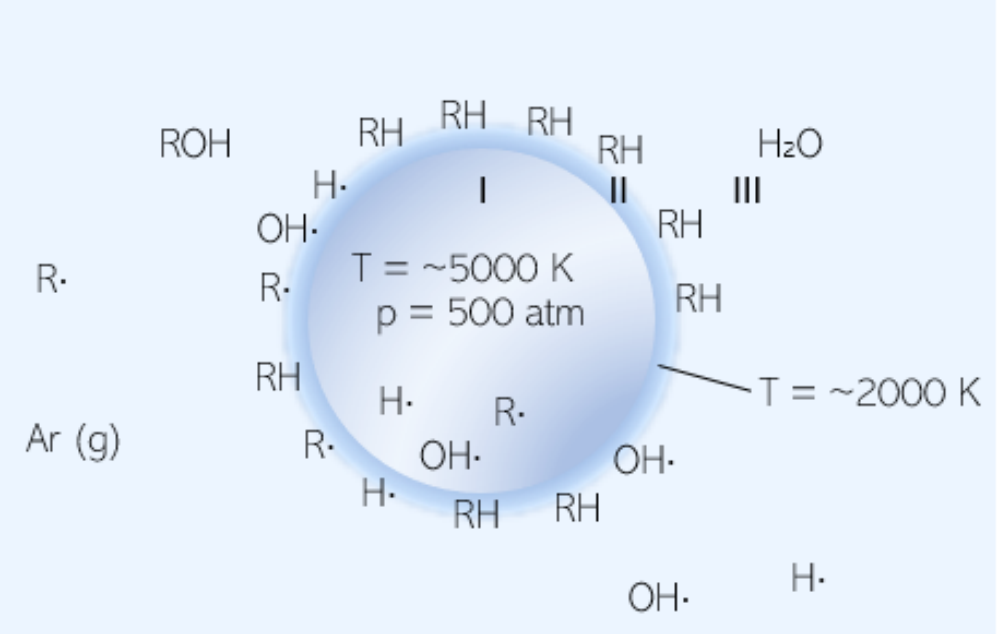

Figure 2.5.2: The reaction environment formed by an imploding cavitation bubble (I) gas phase zone in the cavitation bubble interior, (II) microbubble shell, and (III) bulk solution [12].

Primary radicals, hydrogen radicals (·H), and hydroxyl radicals (·OH) are generated by homolytic splitting of water. The splitting of molecules it is mediated by ultrasound is called sonolysis. The sonolysis reactions of water are shown in the following reaction equation [12].

$$H_2O \xrightarrow{)))} \cdot H + \cdot OH$$

Recombination of hydroxyl radicals may occur according to the following chemical reactions.

$$\cdot OH + \cdot OH \longrightarrow H_2O_2$$

Recombination of hydrogen radicals may occur according to the following chemical reactions.

$$\cdot H + \cdot H \longrightarrow H_2$$

Recombination of primary radicals can be avoided by using surface active molecules, such as alcohols, which can act as radical scavengers as they form secondary radicals when primary radicals attack them, as shown in the following reaction equation [11].

$$RH + OH\cdot(H\cdot) \longrightarrow R\cdot + H_2O(H_2)$$

Radical formation may also occur by pyrolytic decomposition, where of the interfacially bound surfactants are pyrolyzed during cavitation.

$$RH \longrightarrow OH\cdot(H\cdot) + \cdot CH_3\,\mathrm{etc}\,\cdot$$

Reduction of metallic ions into metal nanoparticles can be achieved by the secondary radicals, which have diffused into the bulk solution, as shown in the following reaction equation [11].

$$M^{n+} + \text{reducing species} \longrightarrow M^0$$

The effect of surfactants on the reduction of Pt^{4+} was investigated by Mizukoshi et al. They suggested that radicals formed by pyrolytic decomposition are involved in the reduction of Pt^{4+}, while secondary radicals and radicals by pyrolytic decomposition are involved in the reduction of Pt^{4+} and Pt^{2+}. They found that the reduction rate of Pt^{4+} depended on the surfactant concentration of certain anionic surfactants. It was found intermediate concentrations of surface active groups yielded optimal reduction rate (4.2.2). The critical micelle concentration (CMC) was found to be optimal for anionic surfactants in the work of Mizukoshi et al., which they attributed to the surfactant being able to attach to the cavitation bubble at concentrations lower than CMC, while being hindered from attaching to the cavitation bubbles due to the formation of bulky micelles for concentrations above the CMC [62].

2.5.1 Sonoluminescence

Light emitted during cavitation bubble collapse is an effect of acoustic cavitation called sonoluminescence (SL). Sonoluminescence is used to visualize the sonochemically active regions, but it also finds application within characterization of the temperature, pressure, and electron density in by employing plasma diagnostics tools. SL has also been used to approximate bubble size and size distribution by measuring the intensity of SL when the liquid is subjected to pulsed ultrasound [63]. The sonochemically active regions are visualized by sonochemiluminescence SCL imaging. SCL characterization is done by adding luminol (3-Aminophthalhydrazide) which reacts with oxidizing radicals produced by sonolysis of water to produce excited-state fluorescing 3-aminophthalate (3-APA) according to the following chemical reaction

$$\text{Luminol} + \text{OH}\cdot \longrightarrow \text{3-APA}^* \longrightarrow \text{3-APA} + \text{light}$$

The visible light emitted by the electronic deexcitation to 3-APA is captured by long exposure imaging [64].

2.5.2 Cavitation Efficiency

Scale-up of sonochemical reactors with optimal sonochemical reaction efficiencies necessitates a comprehensive understanding of the operating parameter's effects on acoustic cavitation. The efficiency of acoustic cavitation for generating radicals and sonochemiluminesence is dependent on the number of active bubbles and the pressure generated during the final stage of collapse [19].

The number of primary radicals formed per energy input for the various reaction volumes (i.e., ultrasonic propagation lengths) are related through the sonochemical efficiency (SE) [11]. (SE must not be confused with secondary electrons) The sonochemical efficiency can be found from equation 2.27

$$SE = \frac{[\text{OH}\cdot]V}{P_{\text{acoustic}}t} \tag{2.27}$$

It is the extreme temperatures, pressures, and rates of temperature change in the order of 10^9 Ks^{-1} that mediate radical formation by sonochemical reactions [56, 65]. Increased reaction efficiency can be achieved by tailoring the sonochemical reaction parameters, such as the acoustic frequency, hydrostatic pressure, acoustic power, ambient temperature, fluid, and ambient gas species to promote more extreme collapse conditions [60].

The maximum cavitation bubble temperature is affected by the ambient gas species. Gasses with low heat conduction (i.e., high specific heat ratio ($\gamma = C_\mathrm{p}/C_\mathrm{v}$) are favored as the heat from implosion is retained better and thereby contribute to the mediation of sonochemical reactions [65]. The relation between maximum cavitation bubble temperature and bubble radius can be estimated from equation 2.28 [66]

$$T_\mathrm{max} = T_0 \left(\frac{R_\mathrm{max}}{R_\mathrm{min}} \right)^{3(\gamma-1)} \tag{2.28}$$

Where $\mathrm{T_0}$ is the bulk temperature of the fluid $\mathrm{R_{max}}$, $\mathrm{R_{max}}$ is the maximum radius the cavitation bubble attains before implosion, and $\mathrm{R_{min}}$ is the minimum bubble radius occurring during implosion. The potential energy released during cavitation increases eith increased $\mathrm{R_{max}}$ [66]. The critical size $\mathrm{R_{max}}$ is determined by the frequency, but frequency is not the dominant factor for sonochemical reaction yield [60]. Frequencies between 200–800 kHz provide the highest radical yield [67]. Increasing the acoustic power at a given frequency should increase the should increase $\mathrm{T_{max}}$ due to an increase in $\mathrm{R_{max}}$, in addition to yielding more cavitation bubbles. Increasing the acoustic power cause a greater change in the acoustic pressure, whereby the difference between $\mathrm{R_{max}}$ and $\mathrm{R_{min}}$ becomes greater [66].
Low bulk temperature is favored for high sonochemical reaction yields, as higher bulk temperatures cause more vapor to diffuse into the bubble, which dampens the implosion[56].

Only a limited amount of work in the literature has been dedicated to scale-up of sonochemical synthesis. Scale-up has mainly been achieved by using multiple parallel reactors [16, 14]. Geometric optimization by increasing the reactor height was studied by Son Y et al. They reported the formation of a larger standing wave field with clear separation of nodal and anti-nodal planes accompanied by increased sonochemical activity toward sonoluminescence with increased reactor height. They attributed the formation of a larger and more stable standing wave field at higher liquid heights to the suppression of acoustic radiative force from the traveling wave. Increased sonochemical activity was thought to be due to cavitation bubbles being transported to the larger and more stable standing wave field by the traveling wave component, where the cavitation bubbles would attain positional stability and undergo repetitive transient or stable cavitation [64]. Asakura and Yasuda investigated the effect of frequency and power for moderately increased reactor volumes by increasing the reactor height and found that larger reactors can provide higher reaction rates by accommodating higher acoustic power and were favorable for avoiding loss of sonochemical activity by bubble coalescence. However, increasing the reactor height will decrease the acoustic pressure as the

ultrasonic wave is attenuated by increased interactions with the medium [18, 19].

2.6 Characterization of Sonochemical Reaction Parameters

2.6.1 Calorimetric Determination of Acoustic Power

Calorimetry is the study of heat transfers due to physical or chemical processes by measurement of changes in state variables accompanying these processes [68]. The acoustic power can be estimated from the equation 2.29 under the assumption that all heat contributions to the measured change in temperature of deionized water sparged with argon are due to acoustic cavitation.

$$P_{\text{acoustic}} = mC_{\text{p}} \left(\frac{dT}{dt} \right)_{t=0} \tag{2.29}$$

Where m denotes the mass of the liquid, C is the liquid's heat capacity, and (dT/dt) is the initial rate of change in temperature over time [69].

2.6.2 Ultraviolet-Visible Spectroscopy for Quantitative Analysis

UV-Vis spectroscopy (UV-Vis) is a technique which utilizes interactions between chemical species and electromagnetic waves in the ultraviolet-visible spectral region, for qualitative and quantitative characterization. Various UV-Vis spectrophotometer configurations are available in the current market, however, they all employ a light source that emits broadband UV-Vis radiation. Specific wavelengths are split from the broadband radiation by a monochromator and a dispersion device. Optical components such as lenses, fiber-optics and mirrors are used to guide the electromagnetic wave through a specific path from the light source to the sample, which typically is a solution in a cuvette. The light is then either transmitted or reflected to a detector.

Beer-Lambert's law as shown in equation 2.30, is used to relate the absorption of light to the concentration of the absorber.

$$A = -log_{10} \left(\frac{I}{I_0} \right) = \epsilon c_{\text{i}} L \tag{2.30}$$

, where the transmitted intensity and incident intensity of the light are given by I and I_0 respectively, ϵ denotes the molar absorption coefficient, c_{i} is the concentration, and L is the irradiation length of the sample.

Sufficient sample dilution and detector sensitivity are two important parameters for attaining accurate UV-Vis measurements with a linear signal response. This is because the number of photons that reach the detector decreases with increased absorbance leading to a low noise-to-signal ratio [70]. The validity of Beer-Lambert's law is maintained if the absorber does not affect other absorbers, the sample is homogeneous medium and not turbid [15].

2.6.3 Titanyl Sulfate Dosimetry for Determination of Sonochemical Activity

Titanyl sulfate dosimetry can be used to find the sonochemical activity for producing primary radicals formed during acoustic cavitation. Primary radicals recombine to form H_2O_2, which forms a peroxotitanium (IV) complex with $TiOSO_4$. The UV-Vis spectra of this complex have an absorption peak at $\lambda = 411$ nm and extinction coefficient $\epsilon = 787$ dm^3 mol^{-1}cm^{-1} [69].

2.6.4 Colorimetric Measurements of Platinum Ion Concentration

A colorimetric method based on the formation of the two platinum iodine complexes $PtI_6{}^{2-}$ and $PtI_4{}^{2-}$, from Pt^{4+} and Pt^{2+}, respectively by addition of KI in excess, as can be seen from the following reaction equations.

$$Pt^{4+} + 6\,I^- \longrightarrow PtI_6{}^{2-}$$

$$Pt^{2+} + 4\,I^- \longrightarrow PtI_4{}^{2-}$$

An absorbance peak of $PtI_6{}^{2-}$ can be obseved at $\lambda = 495$ nm ($\epsilon = 9400$ dm^3 mol^{-1}cm^{-1}) and at $\lambda = 388$ nm for $PtI_4{}^{2-}$ ($\epsilon = 5500$ dm^3 mol^{-1}cm^{-1}nm) [11, 62, 71].

2.7 Nucleation and Growth in a Sonochemical System

The importance of reproducible size and surface area for achieving nanoparticles with high catalytic activities has been highlighted in previous sections. Therefore, a thorough understanding of crystallization in a sonoreactor environment is essential for achieving nanoparticles with an optimal surface area.

Classical nucleation theory (CNT) explains the formation of a solid phase due to the influence of thermodynamic effects. CNT states that a supersaturated system will crystallize to lower its free energy. A solution in which the solute concentration is above the solubility limit of the system is said to be supersaturated. The solution system can be divided into three zones characterized by the tendency of the solute to undergo spontaneous crystallization. Crystallization will not occur in the stable zone when the concentration is below the solubility limit. Crystallization can occur in the metastable zone located above the solubility limit. Variations of synthesis parameters such as temperature and concentration can be used to control the crystallization process in the metastable zone. When crossing the supersolubility line, one enters the labile zone in which control of the particle properties is hindered by sudden crystallization [15].

An illustration of the three zones divided by solubility lines an endothermically dissolving solid is presented in Figure 2.7.1

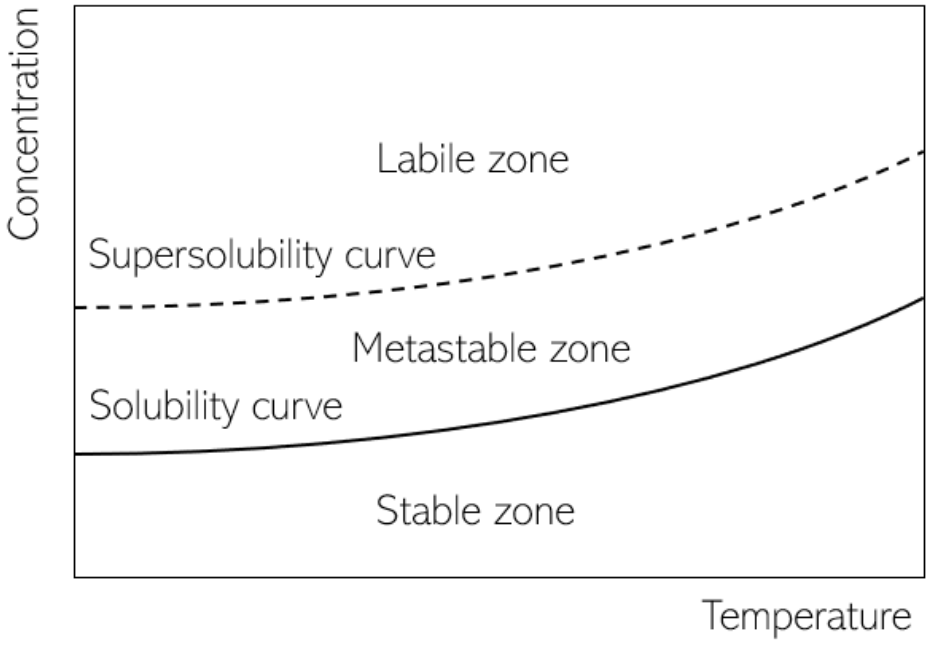

Figure 2.7.1: A graph illustrating the concentration as a function of temperature. The various zones for solution stability are separated by solubility curves. Redrawn with inspiration from [15].

Sonochemical synthesis provides a continuous supply of radicals which is a strong reducing agent [11]. Strong reducing agents commonly promote rapid nucleation, called *burst* nucleation, which promotes small particles with a narrow size distribution. This results in smaller particles because more of the solute is used to nucleate more crystals with less solute available to increase the particle size by growth, and promotes a narrow size distribution as they are grown under the same conditions for a similar amount of time [15].

Power ultrasound has been recognized to increase the rate of nucleation of various inorganic crystals by decreasing the metastable zone and lowering the induction time. Furthermore, ultrasonic synthesis has proven beneficial effects on crystallization by achieving higher yields of crystals at equivalent supersaturations with a more narrow size distribution. There are four main hypotheses for the ultrasonic effect on crystallization. However, the exact mechanisms of nucleation and growth influenced by power ultrasound have yet to be elucidated [72].

(1) Cooling hypothesis
The cooling hypothesis suggests that the liquid surrounding an expanding bubble is cooled, which leads to a local increase in supersaturation that lasts for a brief period of time due to the reduced solubility of the solid.

(2) Pressure hypothesis

The surrounding liquid of a collapsing cavitation bubble is subjected to immense pressure. Species that are less dense in solute form compared to the solid form exhibit decreased solubility and, thereby, higher supersaturation favoring nucleation when subjected to increased pressure. (3) Evaporation hypothesis
The evaporation hypothesis suggests that the local increase in supersaturation could be due to high solute concentration close to the bubble wall as the solvent may evaporate into the cavitation bubble and leave behind a layer depleted of solvent.

(4) Acceleration hypothesis
The cavitation bubble accelerates rapidly at the end of its collapse. It is suggested that this may lead to the segregation of the solute and precursor species over a short time interval, which could increase the nucleation kinetics [72].

Wet chemical synthesis routes tend to exhibit rapid nucleation. The solute concentration is lowered as nuclei form. Eventually, the concentration becomes too low to overcome the energetic barrier for nucleation, and the remaining supersaturation is used to grow the particles. Larger crystals can grow by attachment of monomeric units supplied by smaller crystals by the Ostwald ripening mechanism due to the increased solubility of smaller particles [72]. Aggregation is another size enlargement process in which the high-energy surfaces of nanoparticles become more stable by physical attraction forces between particles which cause them to cluster together reversibly [15].

2.8 Physical Characterization of Catalyst

2.8.1 X-ray Diffraction Characterization of Spherical Nanoparticles

X-ray diffraction (XRD) is a physical characterization technique used for phase identification of crystalline and certain amorphous solids as well as qualitative analysis of crystallite size, lattice constants, and strain, and is sometimes used to elucidate the morphology of bulk and nanoscale materials [73]. X-rays are electromagnetic waves with wavelengths in the order of 1 Å, making them excellent probes for interatomic distances [74]. The working principle of an X-ray diffractometer uses a large electric potential difference to accelerate electrons towards an anode, typically made of Cu or Mo, inside a vacuum tube. The impact from the incoming electrons causes the electrons in the anode material to undergo electronic transitions. X-ray radiation used for XRD analysis is generated from the excess energy released during the relaxation of ejected inner shell electrons. The X-ray wavelength depends on the anode material, as the energy difference for electronic transitions between the higher and lower energy levels differs for every element [75].

Crystalline materials consist of atoms in repeating arrangements called a lattice. The Miller indices "hkl" indicates the position of the crystallographic planes. Parallel planes are separated by an equidistant interplanar distance d_{hkl}. X-ray photons are scattered by elastic collisions with electrons of atoms of the crystallographic planes. Elastic scattering is the interaction of the electromagnetic field of the incoming X-ray, which causes electrons in the specimen to oscillate, having the same period as the X-ray beam. An electromagnetic field of the same phase and wavelength as the incident X-rays, termed a scattered wave, is emitted by the oscillating electrons [74, 76].

X-rays scattered by parallel planes will have a difference in path length. At certain angles, the path length difference is an integer multiple of the wavelength, which causes constructive interference, which yields a signal intensity maxima. Constructive interference can be related to the interplanar distance by Bragg's law presented in equation 2.31

$$\lambda = 2d \sin \theta \tag{2.31}$$

Where the diffraction angle, 2θ, is the angle between the incoming and scattered X-rays. It is the detection of the signals of maximum intensity that are observed as a peak in the X-ray diffractogram. It follows from the Bragg equation that interplanar distance is found from the peak position in the diffractogram, whereas crystallite size can be found from the peak shape [74].

The infinite periodicity of atoms assumed for crystal lattices no longer holds for nanoparticles. There will not be enough lattice planes to give rise to constructive interference with a sharp peak in the diffractogram [77, 73]. Peak broadening is, therefore, a size effect of crystallites with nanoscale dimensions. However, peak broadening can also be due to instrumental effects. Peak broadening and low signal-to-noise ratios make XRD characterization of particles with crystalline domain sizes smaller than 5 nm challenging [73].

Peak broadening due to size effects can be described by the Scherrer equation 2.32 by relating the crystalline domain size, D, to the peak width β at the full width at half maximum (FWHM), of the peak.

$$D = \frac{\kappa\lambda}{\beta cos(\theta)} \tag{2.32}$$

Where θ is the diffraction angle, κ is the Scherrer constant, which is assumed to be 0.89 for spherical particles, and the X-ray wavelength, λ, depends on the anode material used [74, 73].

Particles can be single or polycrystalline, therefore, not necessarily the same as the crystalline domain size. If the Scherrer crystallite size corresponds well to the average particle size obtained by complementary characterization, it could indicate that the sample consists of a population of single crystal particles [73].

Lattice contraction is another size-dependent property of nanomaterials. Nanoparticles' large surface area-to-volume ratios entail that surface atoms have lower coordination numbers, meaning that they have unsaturated bonds. Lattice contraction occurs due to surface relaxation as the surface atoms experience a pull inward from the interior atoms [78].

2.8.2 Electron Microscopy

Electron microscopes utilize an electron source situated at the top of the microscope to emit a beam of high-voltage electrons (5-100 KeV). A positive potential is then used to accelerate the electron beam in a high vacuum through the microscopy column. Electromagnetic lenses and apertures in the column are used to focus the electron beam into a highly focused electron probe. Electrons can be classified as ionizing radiation, which entails that inner-shell electrons of an atom in a specimen may be removed by energy transfer from the collision with an impinging probe electron [79]. Both the nuclei and the electrons of a specimen scatters electrons, causing direct scattering as opposed to X-ray scattering due to interactions of electromagnetic fields [76]. The interactions of electrons with matter generate secondary signals from the specimen, which can be detected and used for qualitative and quantitative analysis [79].

2.8.2.1 Scanning Transmission Electron Microscopy

Scanning transmission electron microscopes (S(T)EM) is a type of electron microscopy in which the primary electron beam penetrates the sample as it is scanned in a raster pattern over the sample surface. The penetration depth is determined by the sample's material composition and the incident electron's energy. Beam electrons are scattered elastically and inelastically as they interact with the sample electrons. Beam energy, incidence angle, and sample composition determine the volume of the sample where the interactions take place, known as the interaction volume. The primary beam's size and interaction volume determines the resolution. Information avout the sample composition can be interpreted from signals generated from back scattered electrons (BSE), which are electrons that are elastically scattered from the sample. Signals of secondary electrons (SE) are due to inelastic scattering. The excellent surface topography imaging by secondary electrons is due to the low escape depth, which is about 1 nm for metals. Other interactions also generate secondary electrons, however, these are usually not of interest. Some of the electrons are transmitted through the sample. Unscattered electrons that are transmitted are used for bright-field (BF) imaging, whereas transmitted electrons scattered at a high angle are used for dark-field (DF) imaging [79, 80, 15].

A scanning electron microscope can be used to determine the elemental composition of a sample by Energy-Dispersive X-Ray Spectroscopy (EDS) characterization. Impinging electrons from the SEM probe current may eject an electron from the nucleus shell to a higher electron shell. Deceleration of electrons from the higher electron shells causes the emission of an X-ray continuum, while filling electron holes by higher shell electrons generates X-ray characteristic for a specific element, as the difference in energy levels varies with atomic number [81].

2.8.2.2 Transmission Electron Microscopy Characterization of Particle Size and Crystallinity

Transmission Electron Microscopy (TEM) is a versatile characterization method. It can be used as a supplementary characterization method or XRD to asses the crystallinity and size of a specimen. Incident beams of electrons from the electron probe will either be scattered or pass through the specimen unaffected. Transmission of enough electrons to be detected necessitates that the sample must be adequately thin. The electrons exiting the specimen will have a non-uniform distribution due to the various scattering interactions. Diffraction patterns originate from the angular distribution of scattered electrons. Diffraction patterns are used to generate electron microscopy images from which one can characterize the particle morphology and size, whereas image contrast is due to the spatial distribution of the scattered electrons. A diffraction pattern analogous to XRD can be observed as spots and lines which relate to the crystallographic attributes of the specimen, [79].

2.8.3 Brunauer-Emmet-Teller Characterization

Physisorption of argon or nitrogen is used as a probe molecule to determine the surface area and pore structure of a catalyst. The gas is adsorbed on the sample surface at its boiling point, T_b, which is 77 K for N_2. The surface area of the sample can then be determined from the cross-sectional area of closely packed physisorbed N_2 molecules utilizing that each adsorbate molecule occupies an area, A_0, which is 0.162 nm^2 for N_2 [33]. The BET equation describes multilayer adsorption and is presented in equation 2.33.

$$\frac{P}{V_\alpha(P_0 - P)} = \frac{1}{\chi V_0} + \frac{(\chi - 1)}{\chi V_0}\frac{P}{P_0} \tag{2.33}$$

Where V_α denotes the volume of the gas adsorbed, and V_0 is the volume of the first monolayer, P is the pressure, P_0 is the saturated vapor pressure of the gas, V_m is the volume adsorbed equivalent to a monolayer of gas coverage [33].

The volume of the adsorbed gas in the first monolayer is given by $V_0 = 1/(\alpha + \chi)$, which can be found by plotting $P/[Va(P_0 - P)]$ as a function of P/P_0 and knowing that the y-intercept is equal to $\eta = 1/\chi V_0$.The surface area of the adsorbate is found by relating V_0 to the number of molecules adsorbed in the first monolayer, through the relation $N_0 = PV_0/kBT$. The total surface area is given by $A = N_0 A_0$ [33].

The underlying assumptions are dynamic equilibrium between adsorbate and adsorptive, equivalence of adsorption sites for molecules constituting the first layer, negligible interactions between the adsorbate molecules, that the heat of adsorption for the first layer is independent of the consecutive layers, which all have the same heat of adsorption that equals the condensation energy, and that the thickness of the multilayer becomes infinite at saturation pressure ($P = P_0$) [33].

2.8.4 Thermogravimetric Analysis for Catalyst Loading Determination

Thermogravimetric analysis (TGA) is a form of thermal analysis commonly used to determine catalyst loading on a support material. The mass of the sample will change as it is heated according to a temperature program with a controlled inert or reactive gas atmosphere. The temperature is measured by a thermocouple in direct contact with the sample crucible. The change in mass is continuously measured as a function of temperature, and the catalyst loading is determined by measuring the mass of the sample before and after the support is burned of [82].

CHAPTER

THREE

EXPERIMENTAL PROCEDURE

3.1 Overview of Experimental Activities

A flow chart providing an overview of the experimental activities performed in this thesis work is presented in Figure 3.1.1. The sonochemical reaction parameters focused on scale-up were investigated and optimized before commencing catalyst synthesis. The precursor salt concentration and sonication time were altered during synthesis. The supported catalyst was separated from the reaction solution in a simple post-processing step, which consisted of filtering, cleaning, and air-drying. Physical and electrochemical characterization was then performed to investigate the reproducibility of the particle properties and catalytic activity of the sonochemically synthesized Pt/XC72.

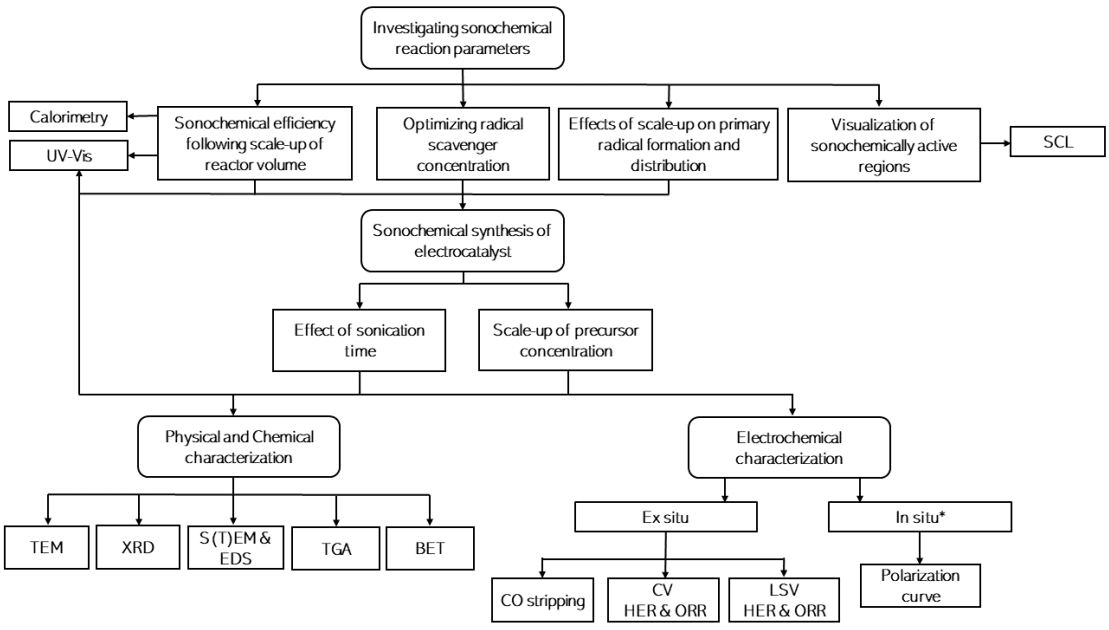

Figure 3.1.1: Flowchart providing an overview of experimental activities.

3.2 Sonochemical Reactor Setup

A pictorial diagram of the sonochemical reactor set-up utilized in this work is shown in Figure 3.2.1. The sonochemical set-up consisted of a cylindrical sonochemical reactor made out of glass mounted on top of a 346 kHz (PZT) ultrasonic plate transducer (70 mm Ø) produced by Honda Electronics. The transducer plate was made from a stainless steel alloy (SUS304). A signal generator, AG1012 from T&C power conversion, was used to supply 50 W electrical power for all experiments. Correction of the impedance discrepancy between the signal generator (50 Ω) and the plate transducer (213 Ω) was achieved by an impedance matcher T1K-7A also from T&C power conversion. The reaction solution was in direct contact with the transducer plate during synthesis. A silicone ring was used to seal the connection between the sonochemical reactor and the transducer plate. A compact recirculating chiller from QSonica was used to maintain the reaction temperature of 3°C by water cooling. The cooling water inlet and outlet were situated at the cooling jacket's lower right and upper left, respectively. Gas supply and additional instruments could be attached through glass adapter cones on top of the sonochemical reactor.

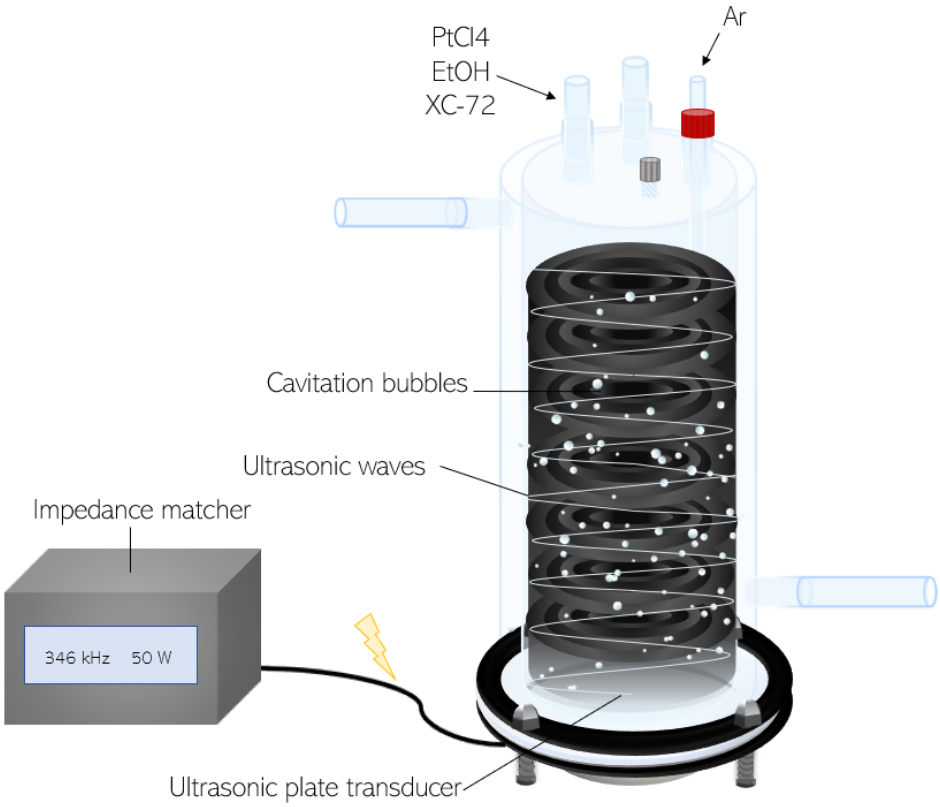

Figure 3.2.1: A simplified pictorial diagram of the sonochemical reactor alongside the signal generator and impedance matching unit. A 346 kHz ultrasonic plate transducer driven at 50 W electric power input is used to synthesize Pt/XC72 catalyst form an aqueous reaction solution consisting of the precursor salt, $PtCl_4$, ethanol as a radical scavenger. The reaction solution was bubbled with Ar-gas (5.0) before and during synthesis. The catalyst support, Vulcan XC-72, should be added at a late stage of the synthesis time.

3.3 Chemicals

Platinum tetrachloride ($PtCl_4$) (Sigma Aldrich, 96 %), (VULCAN ® XC72 carbon black, Cabot Corp.), Ethanol (EtOH) (VWR, 96 % GPR RECTAPUR®), potassium iodide (KI) (Sigma Aldrich, $\geq$ 99 % ACS reagent), titanium(IV) oxysulfate solution ($TiOSO_4$) (Sigma Aldrich, 1.9-2.1 %), luminol (3-Aminophthalhydrazide, 5-Amino-2,3-dihydro-1,4-phthalazinedione) (Sigma Aldrich $\geq$ 97%), Nafion^{TM} 117 containing solution $\geq$ 5% (Tetrafluoroethylene-perfluoro-3,6-dioxa-4-methyl-7-octenesulfonic acid copolymer), sulphuric acid 0.5 M (H_2SO_4) diluted from (Sigma Aldrichfrom, 95-98%, Sodium hydroxide (NaOH) (Sigma Aldrich, reagent grade, $\geq$ 98%, pellets (anhydrous)) EMPROVE® ESSENTIAL, Ph. Eur., BP, JPE, NF) and Milli-Q water (18.2 M$\Omega \cdot$ cm).

3.4 Sonochemiluminescence Procedure

The sonochemically active zones in a small (200 mL) and a large (800 mL) reactor volume were visualized by SCL imaging of luminal solutions, which are colored blue during sonication, as elaborated upon in Subsection 2.5.1. The luminal solution was prepared by the addition of 1.0 gL^{-1} NaOH and 0.1 gL^{-1} luminol in Milli-Q water. The purpose of NaOH is both to enhance the weak light emitted by SCL by providing additional OH species and promote the dissolution of luminol. The used luminal solution was exchanged with a new solution in between imaging of each volume. The SCL images were captured by a digital single-lens reflex camera (Canon EOS 500D) using a 50 mm lens. The camera settings were optimized for long-exposure imaging using raw image file format to avoid processing by the image sensor, a high ISO value, lens aperture of f/4.5, and a long shutter speed (30 seconds). The distance and position between the sonochemical reactor and the camera were kept constant by a tripod. A cardboard box in a room without artificial lighting and closed window blinds was used to remove as much superfluous light as possible. However, a completely dark room would have been preferred to avoid light contamination of the SCL images.

3.5 Titanyl Sulfate Dosimetry Procedure

The effect of increased ultrasonic radiation height (i.e., volume) on primary radical yield was characterized by titanyl sulfate dosimetry, as explained in Section 2.6.3. Three repetitions were performed for the following reactor volumes 200 mL, 300 mL, 400 mL, 600 mL, 700 mL, and 800 mL. The first repetition was conducted during the specialization project, while subsequent repetitions were performed during the master's thesis work. A measurement of a 200 mL and an 800 mL reactor was conducted by co-supervisor Henrik Erring Hansen. All measurements were performed in a sonochemical reactor with Milli-Q water sonicated with a frequency of 346 kHz and supplied with 50 W electrical power. The water was purged with Ar-gas (5.0) for 20 minutes before sonication and was maintained throughout the entire duration of the measurement. Water cooling was used to maintain a reaction temperature of 3 °C. A line was drawn on the outside of the reactor marking the height of the water meniscus at 200 ml, 450 ml, and 800 mL. An autopipette extended with a plastic tube and glass pipette had to be used to extract samples of the solutions due to the tall reactor height. The reproducibility of the amount of solution extracted by the modified pipette set-up was investigated by weighting consecutive samples using an analytical balance. A 500 μL sample of the solution at one of the standardized liquid heights every 5 minutes for 20 minutes. The addition of 500 μL $TiOSO_4$ 0.02 M solution was done using the same autopipette set-up before mixing the $TiOSO_4$ solution with the water sample in a cuvette. The absorbance of the peroxotitanium (IV) complex (λ = 411 nm and $\epsilon = 787\,dm^3mol^{-1}cm^{-1}$ [83]) was measured by UV-Vis spectroscopy (Thermo Scientific Evolution 220 UV-Vis spectrophotometer) over a wavelength range of 300-600 nm with a scan rate of 100 nm/min.

Titanyl sulfate dosimetry was also used to investigate the distribution of radicals in a reactor filled with 800 mL Milli-Q by collecting samples at three heights 5.2 cm, 11.7 cm, and 20.8 cm.

3.6 Sonochemical Synthesis of Pt/XC72

Pt-nanoparticles on a carbon black support with a nominal loading of 20wt% (Pt/XC72 20wt%) were synthesized sonochemically. A total of thirteen Pt/XC72 batches were synthesized. Three by three syntheses series were carried out with XC72 added from the start and precursor concentrations of 0.4 mmol dm^{-3}, 0.6 mmol dm^{-3}, 1.0 mmol dm^{-3} $PtCl_4$ (99.9% metal basis Sigma Aldrich) in a 900 mL reactor. A fourth synthesis series with XC72 added during the final stage of the sonication time was done using 0.4 mmol dm^{-3} and 0.6 mmol dm^{-3} in 900 mL reactor, and 1.2 mmol dm^{-3} $PtCl_4$ in an 800 mL reactor. Co-supervisor Henrik Erring Hansen synthesized Pt/XC72 using 1.0 mmol dm^{-3} $PtCl_4$ in a 200 mL reactor, with XC72. An overview of the syntheses series showing the variation in reaction parameters of precursor salt concentration, sonication time, XC72 addition, and reactor volume is given in Table 3.6.1. Henceforth the reaction parameters used will be implied the by referring to the synthesis series in question.

Table 3.6.1: Synthesis series showing the variation in reaction parameters.

No.	Concentration of $PtCl_4$ (mM)	Synthesis time (hr)	XC72 addition (hr)	Reactor volume (mL)
Synthesis Series 1				
1	0.4	2	0	900
2	0.4	3	0	900
3	0.4	3.5	0	900
Synthesis Series 2				
4	0.6	4	0	900
5	0.6	5	0	900
6	0.6	8.5	0	900
Synthesis Series 3				
7	1.0	13	0	900
8	1.0	13	0	900
9	1.0	13	0	900
Synthesis Series 4				
10	0.4	4	3.75	900
11	0.6	6.5	6.25	900
12*	1.2	6	5.75	800
Synthesis Series 5 (Produced by Henrik Erring Hansen)				
13	1.0	1	1.67	900

The precursor solution was prepared by adding 0.5 mol dm^{-3} 96% ethanol, used as a radical scavenger, to a round flask. The optimal concentration of ethanol as a radical scavenger was determined by colorimetry. Then the amount of XC72 needed to achieve a nominal catalyst loading of 20wt% was added to the ethanol for synthesis series 1, 2, and 3, in which XC72 was added at the start. The solution was magnetically stirred for 10 minutes before being sonicated in an ultrasonic bath for 15 minutes. Similarly, the required amount of $PtCl_4$ was weighted and added to the solution and mixed in an ultrasonic bath for an additional 15 minutes. The precursor solution was poured into the sonochemical reactor from one of the

inlets at the top. Any residual lumps of black were redispersed in Milli-Q water in an ultrasonic bath. Milli-Q water was added to the sonochemical reactor until the precursor solution volume of 900 mL was achieved. A similar procedure was followed for synthesis series 4 and 5, except 100 mL XC72 solution was instead added.

Ar-gas (5.0) was supplied just below the solution-air interface for 20 minutes before synthesis to remove dissolved gasses and throughout the synthesis to promote cavitation collapse conditions. Isothermal conditions of 3 C were maintained by water cooling. The applied acoustic frequency was 346 kHz, and 50 W electric power was supplied. The acoustic power was previously determined to be (42 ± 2.4) W from the specializations project work. The reaction time was found experimentally by observing when the decrease in absorbance peaks from UV-Vis spectra corresponding to the reduction of Pt^{4+} and Pt^{2+} did not change significantly with time.

The sonicated solution was poured into a round flask, and Pt/XC72 was separated by filtering using a Supor ® 800 0.8 μm 90 mm membrane filter from Pall corp. in a Buchner funnel. The filter cake was washed three times with ethanol 96% and then three times with Milli-Q water to remove contaminants. The filter cake was air-dried for two days. Finally, the Pt/XC72 filter cake was scraped off the filter and ground into a fine powder using a mortar and pestle.

3.6.1 Calorimetry Procedure

Calorimetric measurements were performed as a part of the specialization project in the fall of 2022. A Fluke 289/287 thermocouple situated in the middle of the reactor volume was used for calorimetric measurements of Milli-Q water . Reactor volumes of 200, 400, 600, 800, and 900 mL were sonicated for two minutes by applying an acoustic frequency of 346 kHz and 50 W. Three repetitions were conducted for each volume, and the water was exchanged between every repetition.

3.7 Colorimetry Procedure

Colorimetric measurements of the extent of reduction and reaction kinetics of Pt^{4+} and Pt^{2+} into metallic Pt were performed during synthesis. This was done by collecting 125 µL $PtCl_4$ solution samples and mixed 125 µL KI 0.432 mol dm^{-3}. The sample solution was diluted with 750 µL Milli Q water and vortexed to achieve good dispersion to ensure the validity of Beers-law 2.30. The sample was extracted with a syringe and filtered with a 0.2 µm (PTFE arcodisc syringe filter) to remove XC72 and Pt particles before being transferred into a cuvette. The absorbance of the $PtI_6{}^{2-}$ complex (λ = 495 nm and ϵ = 9400 (dm^3/molcm) and the $PtI_4$2-[11]) complex (λ = 388 nm and ϵ = 5500 (dm^3/mol/cm)[11]) was measured over a wavelength range from 200-800 nm by a UV-Vis spectrophotometer (Thermo scientific evolution 220 spectrophotometer) with a scan rate of 100 nm/min and a resolution of 1 nm. Sensible sampling frequencies were found by trial and error. The first synthesis of synthesis series 1, 2, and 3 were sampled at every minute during the first 5 minutes before being sampled with longer time intervals, typically 30 minutes, 1 hour, or 2 hours until there was no significant change in absorbance complete reduction.

3.7.1 X-ray Powder Diffraction Procedure

X-ray diffraction (XRD) characterization of the phase purity and mean crystallite size of the Pt/XC72 catalyst was performed with a Bruker D8 A25 DaVinci X-ray Diffractometer with a Cu K-α radiation source (λ = 1.5406 [77]. The samples were prepared by adding Pt/XC72 catalyst to a Si-cavity 10 mm and covered with a Kapton film to prevent instrument contamination and user exposure. The instrument operated with Bragg-Brentano geometry measuring over a 2θ angular range of 15°75°, a scan rate of 0.044° per minute and a 0.3° fixed slit for 1 hour. The DIFFRAC.EVA software from Bruker was used to compare the measured diffractograms to reference diffractograms. Contributions to the diffractogram from the broad peak due to amorphous XC72 were fitted using an SPVII statistical function before evaluating the Lorentzian crystallite size. Determination of the Lorentzian crystallite size was evaluated by the integral breadth method by Pawley refinement, using a 4^th order Chebyshev background polynomial in the DIFFRAC.TOPAS software from Bruker.

3.7.2 Scanning Transmission Electron Microscopy Procedure

The size and morphology of Pt/XC72 were investigated by secondary electron and bright field imaging modes acquired with a Hitachi High-Tech SU9000 electron microscope operating at an acceleration voltage set to 30 kV. Additional qualitative analysis and visualization of the dispersion were obtained by an EDS detector (Oxford Ultim Extreme 120 mm2 SDD detector). Samples were prepared by dispersing a very small amount of Pt/XC72 in a solution consisting of equal parts Milli-Q water and ethanol(96%), using an ultrasonic bath, and then drop casting 5 µL onto a Formvar, carbon-coated Cu TEM-grid. The samples were covered by a watch glass to avoid contamination of dust particles and let to air dry.

3.7.3 Transmission Electron Microscopy Procedure

The same samples used for S(T)EM were used for TEM. Transmission electron microscopy (JEOL JEM2100 TEM) was conducted by an operator at the TEM Gemini Centre in Trondheim. Various magnifications were used. Overview images by bright field and conventional images used MAG 120k. Close-up images used MAG 500k. Selected-area diffraction patterns (SAED) used a camera length of 20 cm.

3.7.4 Electrochemical Characterization Procedure

The electrochemical surface area was determined by CO-stripping voltammetry and cyclic voltammetry using the H_{UPD} method. Catalytic activity towards the HER and ORR was characterized by linear sweep voltammetry (LSV). The resistance was determined by electrochemical impedance spectroscopy (EIS), which was then used to correct for the iR drop in LSV measurements.

All electrochemical measurements were performed in an electrochemical cell using a three-electrode set-up as described in section 2.3.1, and were recorded with an Ivium-n-stat potentiostat. The electrolyte was an acidic solution of 0.5 mol dm^{-3} H_2SO_4. The solution was bubbled 20 minutes with Ar before characterizing the

HER by CV and LSV. The solution was bubbled for 20 minutes with O_2 before characterizing the ORR. The working electrode consisted of a layer of catalyst ink drop cast onto a rotating disk electrode (RDE) with a geometrical area of $A = 0.196\,cm^2$. The reference electrode (RE) was the reversible hydrogen electrode (RHE), and the counter electrode (CE) was made out of graphite. The GC electrode was prepared by polishing using pads moisturized with Milli-Q water and alumina particle slurries to ensure a clean and smooth electrode surface. Particle sizes of 0.5 µm was used in the first coarse polishing step before a fine polishing step with alumina particle size 0.05 µm and finally, a polishing step on a pad without alumina.

The catalyst ink was prepared by weighing 10 mg Pt/XC72 catalyst in a sample bottle 475 µL Milli-Q water, 475 µL isopropyl alcohol (IPA), and 50 µL Nafion (5wt%), in the listed order. A homogeneous mixture was achieved by magnetic stirring for 10 min before dispersion by sonication in an ultrasonic bath (42 Hz) for 30 minutes. The working electrode of all ex-situ electrochemical measurements was prepared by drop casting 10 µL onto a stationary GC rotating disk electrode and air-dry it for 15 minutes while rotating at 200 rpm.

Electrochemical impedance spectroscopy (EIS) was used to determine the iR-compensation used for LSV measurements, as explained in section 2.3.3. The starting voltage E_{start}, was set to -0.01 V the frequency range was between 10^5-1 Hz, and the current range was set to 100 mA.

Linear sweep voltammetry (LSV) measurements were performed to assess the catalytic performance of the catalyst. This was done by measuring the overpotential needed to obtain a current density of -10 mA normalized over the geometric area of the GC electrode. A scan rate was 1 mV s^{-1} was used to measure the current through the potential range between E_{start} = 0.01 V to E_{final} = -0.1 V, for HER while the potential range for ORR was from 1.2 - 0.02 V. The potential was corrected for the resistance by multiplying the resistance found from EIS by 0.85.

Cyclic voltammetry was used to determine the electrochemical surface area (ECSA) of the catalyst by the H_{UPD} as elaborated upon in section 2.3.4. The working electrode was cycled 20 times between 0.02-1.2 V vs. RHE with a scan rate of 50 mV s^{-1} to achieve a stable voltammogram. Integration over the area approximately between 0.4-0.03 V for the sweep in the cathodic direction from the 20^{th} cycle was used to find the ECSA as described in section 2.3.4. The system was reset in between measurements by cycling with a scan rate of $100\,mV\,s^{-1}$ five times. The solution was bubbled with O_2 for 20 minuted

Additional measurements of ECSA were obtained by CO-stripping voltammetry as explained in the section 2.3.4. Dissolved oxygen was removed from the 0.5 M H_2SO_4 electrolyte by bubbling with N_2. The electrode was preconditioned by recording 150 cycles, with a sweep rate of 100 mVs^{-1} from 0.02 V to 1.2 V until a stable voltammogram was attained.

An additional hydrogen adsorption ECSA measurement was done by recording

20 cycles sweeping from 0.02 V to 1.5 V, with a sweep rate of 50 mVs^{-1} and a rotation speed of 1600 rpm.

A second preconditioning step included recording five cycles from 0.02 V to 1.2 V with a sweep rate of 10 mVs^{-1}, without rotation. Following this step, the N_2 gas supply was disconnected, and CO gas was connected. Then the electrode was saturated with CO-gas by bubbling for 10 minutes while maintaining the potential at 0.05 V to promote good coverage of linearly adsorbed CO onto Pt [37].

Then the solution was bubbled with N_2 gas for 30 minutes to remove CO. The CO-stripping voltammogram included five cycles recorded by sweeping from 0.02 V to 1.2 V with a sweep rate of 10 mV^{-1}. The area under the CO peak from the first cycle was used to determine the $ECSA_{CO}$, and the second cycle was used as a baseline. The three remaining sweeps are carried out to establish that there was no additional CO from the solution that had adsorbed to the electrode.

3.7.5 Brunauer-Emmet-Teller characterization

BET is a method for surface area characterization complementary to the aforementioned voltammetric methods. The working principles of this method is described in subsection 2.8.3. Glass test tubes for BET analysis were kept in a heating cabinet to avoid contamination of moisture from the air. The test tubes had to cool down to room temperature before weighing them to avoid erroneous readings of the mass. About 0.1 g of Pt/XC72 catalyst powder was added to the test tube. A rubber stopper filled the tube opening to avoid nanoparticle contamination. A degassing step was used to remove moisture adsorbed to the Pt/XC72 surface. The samples were degassed with N_2 at 90 °C for 1 hour before being degassed at 250 °C for at least 15 hours with the Degas Smartprep for 3Flex from Micromeritics. The samples were then cooled to room temperature and measured again to see how much weight was lost during degassing. Then the samples were mounted in the TRISTAR 3000 surface area and porosity analyzer for the BET analysis. A cooling bath of 3L liquid nitrogen was used to maintain isothermal conditions during the measurement.

3.7.6 Thermogravimetric Analysis

Thermal gravimetric analysis was performed in a thermal analyzer (NETZSCH STA F3 449 Jupiter) was used to investigate the actual loading of Pt on carbon black (XC72). The methodology behind this characterization method is explained in subsection 2.8.4. The measurements were performed by recording the weight of an empty alumina crucible with a pierced lid. A small amount of catalyst powder (0.5-1.5 mg) was added to the crucible, and the mass of the catalyst was recorded. The crucible should always be handled with forceps to avoid contamination by oils from the skin. The crucible with a pierced lid was placed on the thermobalance. The furnace chamber was purged with Ar-gas three times before commencing the measurement. A synthetic air (N2/O2) atmosphere was maintained by a gas flow set to 20 ml min^{-1}. The sample was heated with a temperature ramp of 10 °C min^{-1} from the initial temperature, T_{int}, of 25 °C up to 800 °C, where it dwelled of 1 hr and 30 min to burn off carbon, before the temperature was brought back

down to T_{int} °C with a ramp of - 10 °C min^{-1}. The crucibles were cleaned in ethanol (96%) in an ultrasonic bath and dried in a heating cabinet.

CHAPTER

FOUR

RESULTS

4.1 Effects of Scale-Up of Reactor Volume

Calorimetry was used to investigate the effect of increased reactor volume, by increasing the reactor height, on acoustic power, $P_{acoustic}$ in the specialization project work. The acoustic power (W) as a function of reactor volume (mL) is shown in Figure 4.1.1.

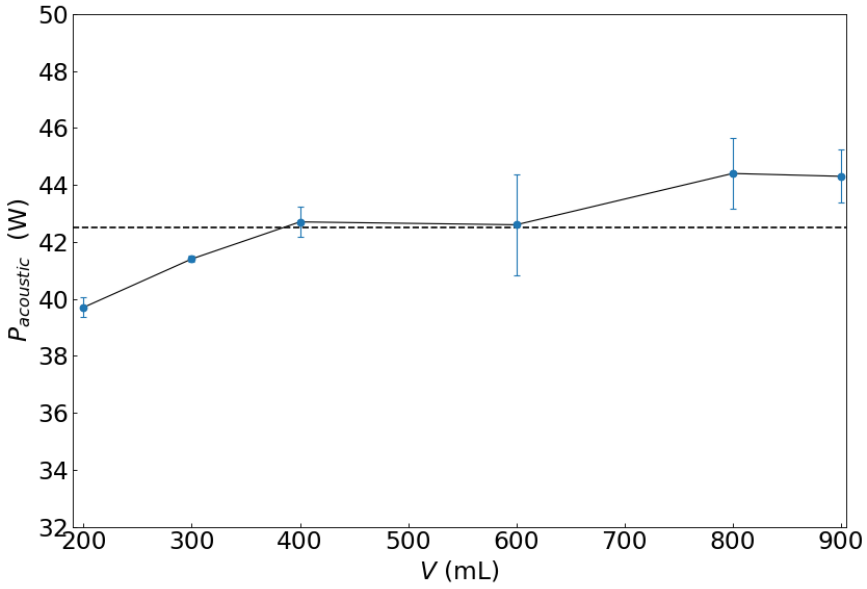

Figure 4.1.1: Acoustic power as a function of reactor volume, with error bars equal to the standard deviations and the dashed line indicating the mean value. The data was obtained by calorimetric measurements performed in the specialization project [31].

A slight increase in acoustic was observed when increasing the reactor volume. The average acoustic power was (42.5 ± 2.4) W [31].

The effect of increased reaction volume on the formation of primary radicals was investigated by titanyl sulfate dosimetry.

The results from titanyl sulfate dosimetry are presented as the rate of formation of ·OH (μmol min^{-1}) as a function of reactor volume (mL) in Figure 4.1.2.

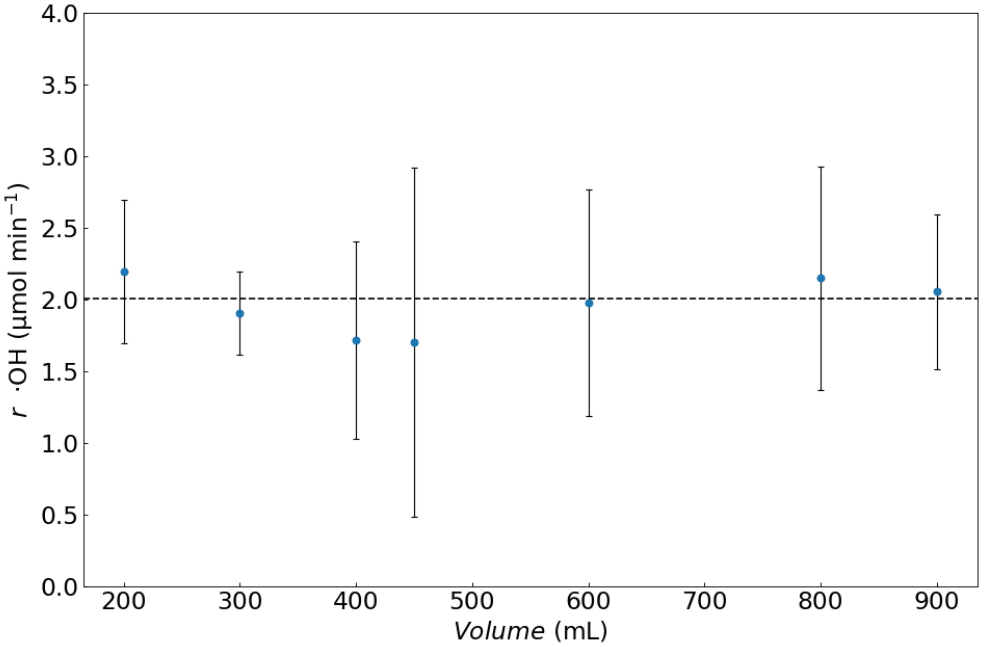

Figure 4.1.2: The rate of formation of ·OH formed as a function of reactor volume. The error bars are equal to the standard deviations, and the dashed line indicates the mean value.

The rate of formation for ·OH was maintained within the experimental error for all reactor volumes. The average rate of formation was $(1.96 \pm 0.23)\,\mu$mol min^{-1}.

However, when taking the acoustic power and volume into consideration, the average initial sonochemical efficiency was found from equation 2.27 to be $0.0011 \pm 0.037\,\mu$mol J^{-1}. Approximate sonochemical efficiencies for longer sonication times were calculated, assuming constant acoustic power. The sonochemical efficiencies as a function of sonication time (hr) for the various reactor volumes (mL) are presented in Figure 4.1.3.

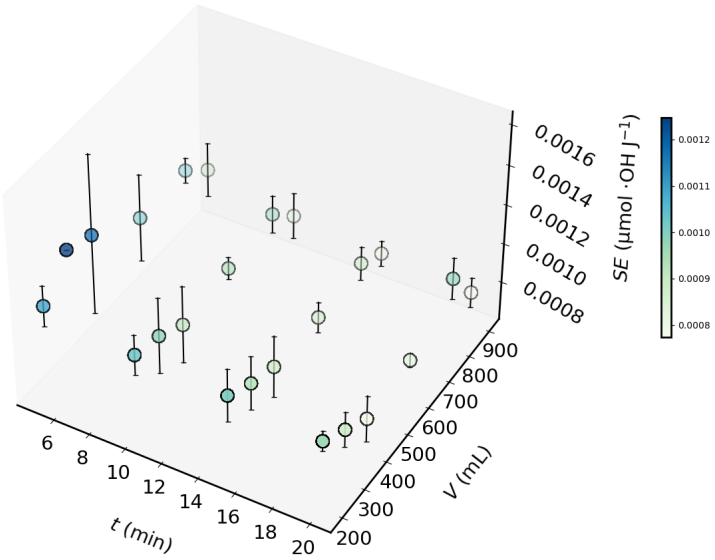

Figure 4.1.3: The sonochemical efficiency for producing ·OH per unit of energy input for various reactor volumes. Assuming constant acoustic power. The error bars are equal to the combined error of the ·OH concentration and acoustic power. It was found that the sonochemical efficiency was within the combined experimental error of ·OH concentration and acoustic power for all volumes.

Titanyl sulfate dosimetry was also used to probe whether experimental variations in sampling height would affect the observed radical formation and if the radical concentration was uniform throughout the sonochemical reactor. The rate of formation of ·OH as a function of sonication time for short (5.2 cm), intermediate (11.7 cm), and elevated (20.8 cm) sampling heights in a reactor filled with 800 mL Milli-Q water is presented in Figure 4.1.4. The concentration of ·OH was found to be within the experimental error for all sampling heights suggesting a homogeneous reaction environment.

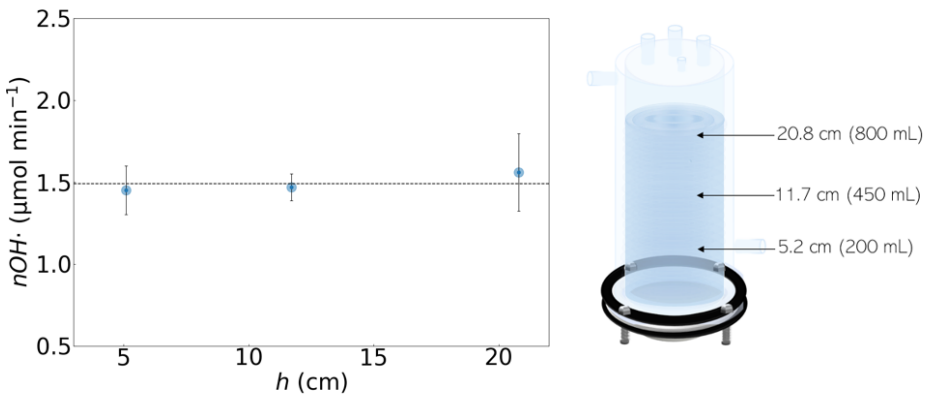

Figure 4.1.4: The rate of formation of ·OH formed as a function of sonication time for various sampling heights in an 800 mL reactor.

The effect of increasing the reactor volume on the sonochemically active areas in a small was visualized by SCL. Figure 4.1.5 shows the sonochemically active areas in a small reactor (200 mL) and a large reactor (800 mL).

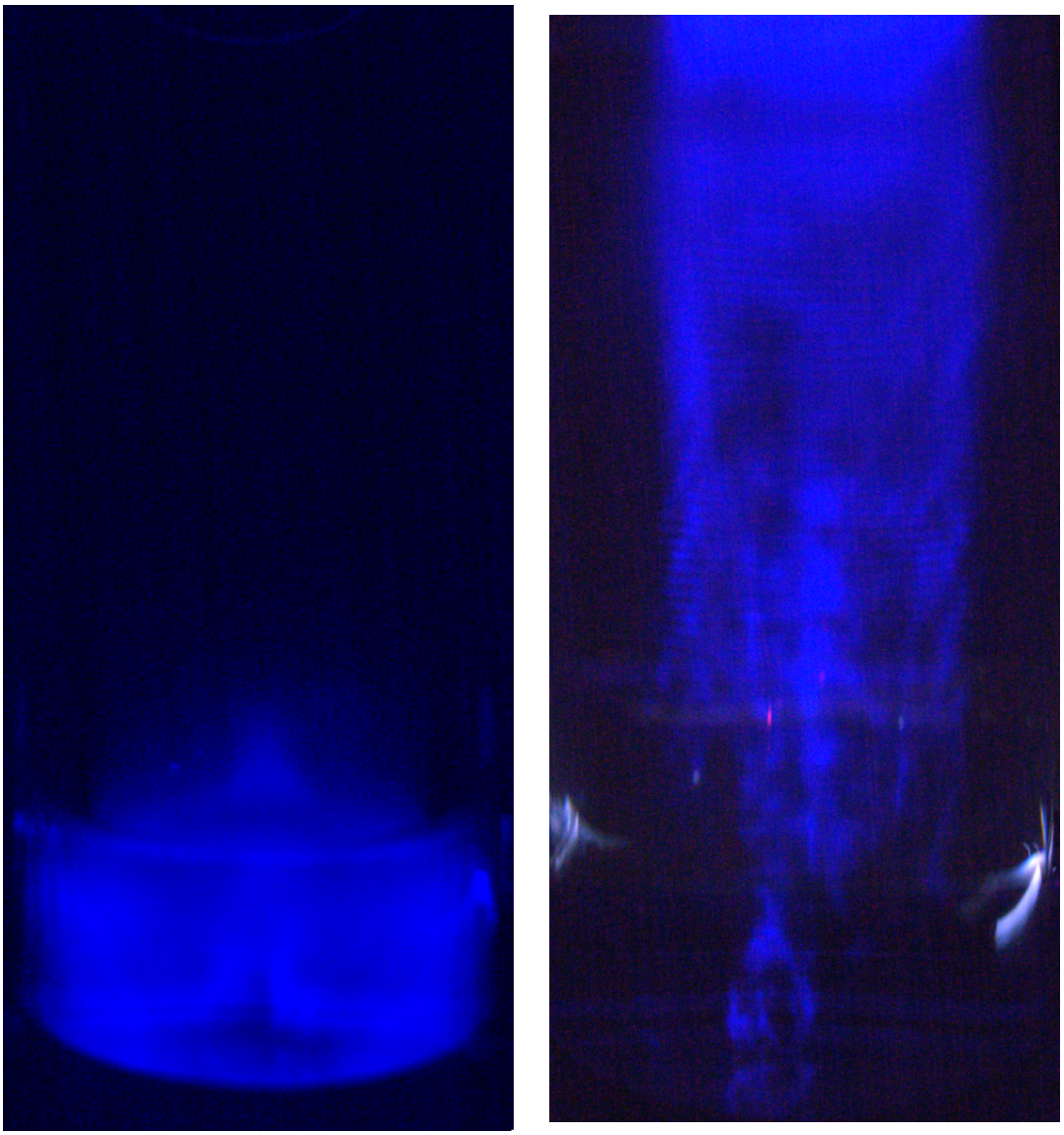

(a) **(b)**

Figure 4.1.5: Visualization of the sonochemically active areas by sonochemiluminesence in a reactor volume of 200 mL (5.2 cm) (a), and 800 mL (20.8 cm) (b). The image exposure time was 30 seconds.

The small reactor seemed to have near uniform sonochemical activity for sonochemiluminesence. No clear separation of a standing wave and traveling wave field was observed in the small reactor, whereas a clear separation of a traveling wave region and a standing wave region with separation of nodal and anti-nodal planes was observed in the large reactor.

4.2 Synthesis

The colorimetric technique described in section 2.6.4 was used to monitor the reduction of Pt^{4+} to Pt^{2+} and further reduction of Pt^{2+} to Pt (s). The absorbance of $PtI_6{}^{2-}$ partially overlaps with the absorbance peak of $PtI_4{}^{2-}$ corresponding to Pt^{2+}. Evaluation of the concentration profile of Pt^{2+} required this contribution to be removed by post-processing. Formation of Pt^{2+} from the reduction of Pt^{4+} occurs predominantly by pyrolytic decomposition, which is dependent on the radical species and concentration, as described in section 2.5. Ethanol 96% was used as a radical scavenger in this work. Colorimetry was first used to optimize the radical scavenger concentration in a 200 mL reactor and then used to monitor the reduction of Pt-ions during synthesis. The UV-Vis spectra of the platinum-iodine complexes are presented in Figure 4.2.1a and Figure 4.2.1b. The resulting concentration profiles of Pt^{2+} for various radical scavenger concentrations are presented in Figure 4.2.2.

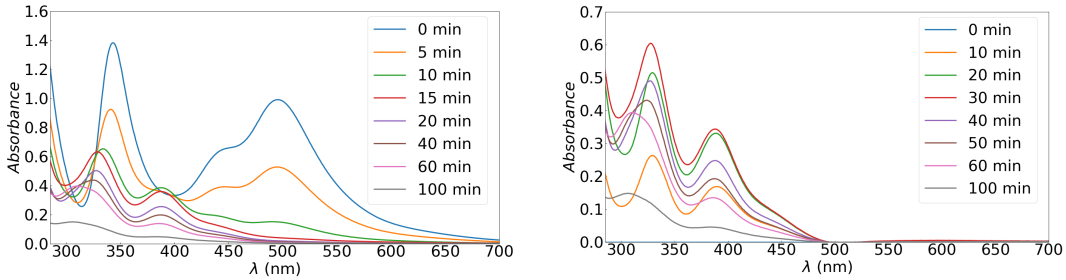

Figure 4.2.1: UV-Vis spectra for a sonochemical synthesis of 1.0 mmol dm^{-3} $PtCl_4$ in a 200 mL reactor (a), and the same corresponding spectra with contributions from Pt^{4+} removed (b).

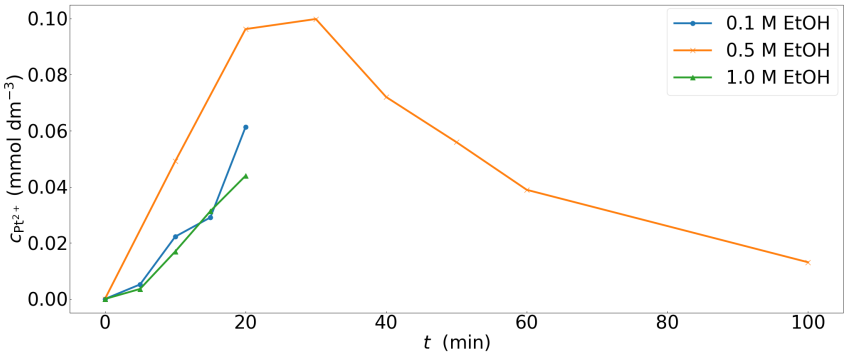

Figure 4.2.2: The concentration profiles of Pt^{2+} reduction for various radical scavenger (ethanol 96%) concentrations in a 200 mL reactor.

It was found that an ethanol concentration of 0.5 mol dm^{-3} yielded the fastest formation of Pt^{2+}. This concentration was therefore used for all syntheses of Pt/XC72 performed in this work.

The change in concentration $Pt^{2+}(mmol\,dm^{-3})$ for the syntheses with XC72 added at the end, and a synthesis with XC72 added at the start is shown in Figure 4.2.3.

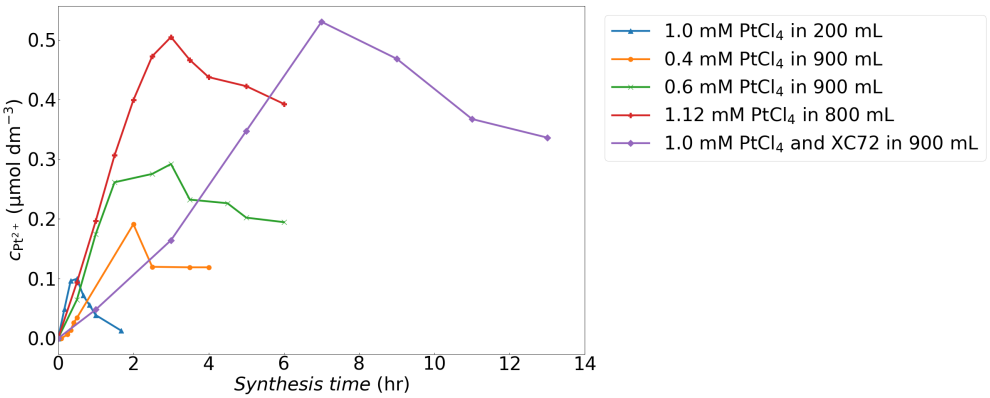

Figure 4.2.3: The concentration profiles of Pt^{2+} reduction for various precursor salt concentrations and reactor volumes, with and without XC72 added at the start of synthesis.

The reduction rate was greater for syntheses without XC72 present from the start, as expected, due to the dampening of ultrasonic waves that are scattered by XC72. The observed increase in the reduction rate of Pt^{2+} is expected as the concentration of the reducing agent increase with reduced reactor volume, as shown through dosimetry measurements.

The real catalyst loading (wt%) obtained by TGA is presented in Figure 4.4.3c as a function of synthesis time(hr).

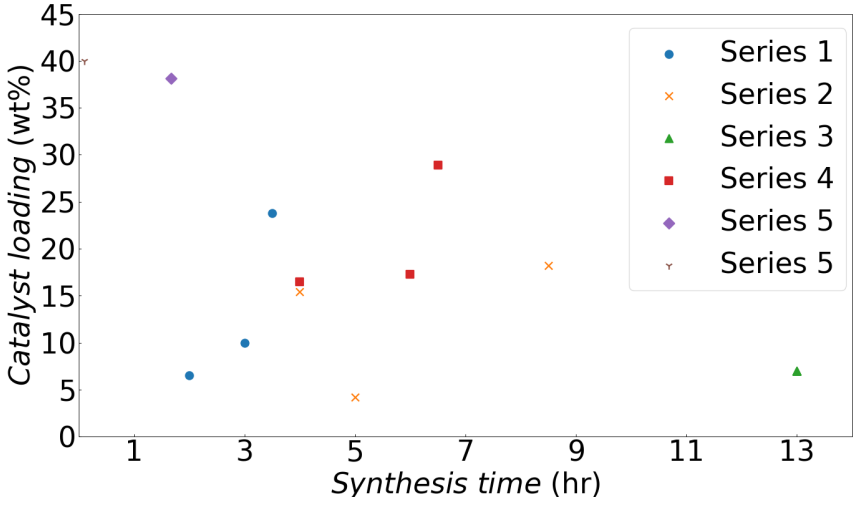

Figure 4.2.4: The real catalyst loading(wt%) obtained by TGA.

The catalyst loading generally increased with synthesis time for synthesis series using the same precursor salt concentration (series 1 and series 2), as would be expected due to more Pt^{2+} being reduced to Pt (s). Synthesis series 4 and 5, in which XC72 was added in the last 15 minutes of the synthesis, exhibited significantly higher catalyst loadings compared to syntheses with XC72 added from the start. The loading of synthesis number 12 (1.12 mmol dm^{-3} $PtCl_4$) was nearly

2.5 times greater than the loading of synthesis series 3 (1.0 mmol dm^{-3} $PtCl_4$), despite synthesis series 3 being sonicated for more than twice as long. Synthesis with XC72 is preferred for achieving higher catalyst loading. The commercial catalyst was standardized to 40wt%, while the Pt loading of the catalyst in synthesis series 3 was assumed from one TGA measurement, as they were synthesized using the reaction parameters.

4.3 Physical Characterization

Phase pure Pt-nanoparticles with a reproducible size and narrow size distribution were achieved in the scale-up of this sonochemical synthesis route. The average particle size was evaluated by hand measurement of at least 150 individual particles by secondary electron imaging and bright field imaging obtained by S(T)EM characterization, as can be seen in Figure 4.3.1a and Figure 4.3.1b, respectively. Crystallite sizes found by XRD are presented in Figure 4.3.1c, and were used to assess whether the particle sizes obtained by S(T)EM were representative of the entire particle population.

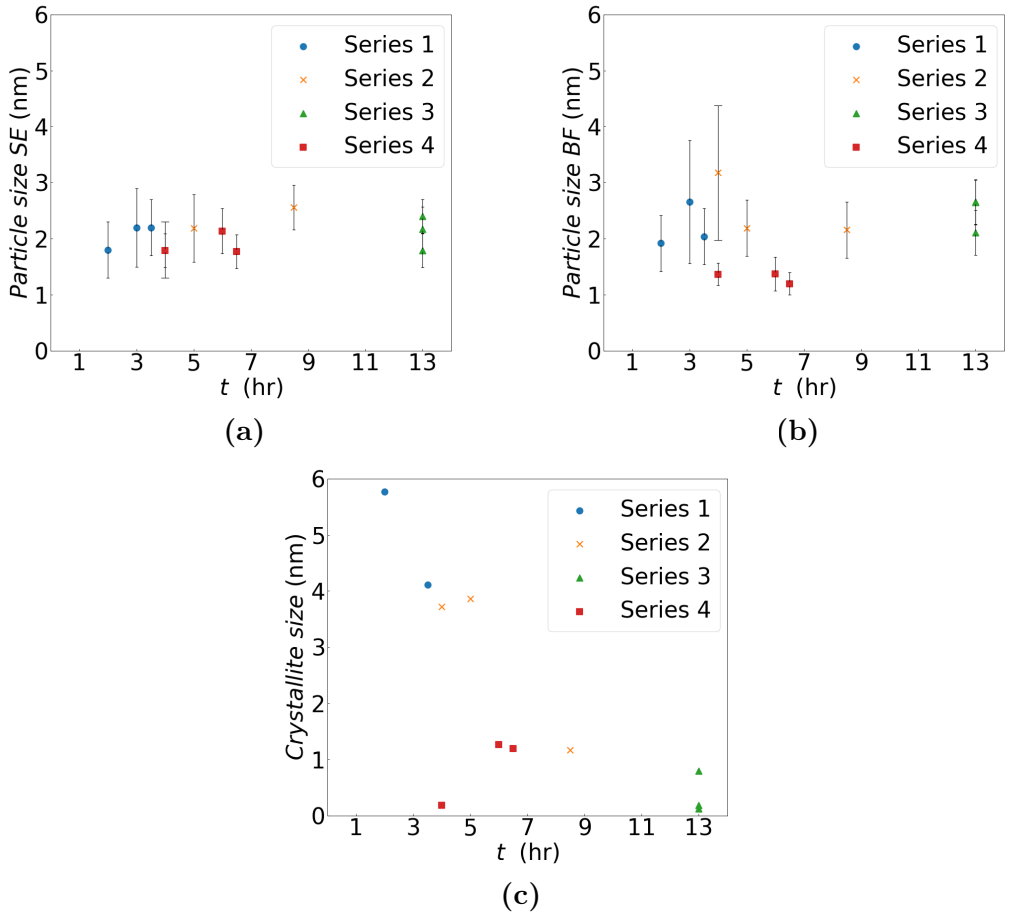

Figure 4.3.1: The average particle size obtained by S(T)EM using (a), secondary electron imaging (b), bright field imaging, and crystallite size obtained by XRD (c).

Representative S(T)EM micrographs obtained by secondary electron (SE) imaging and bright field (BF) imaging of sonochemically synthesized 20wt% Pt/XC72 and commercial chemically synthesized 40wt% Pt/XC72 catalyst and their corresponding particle size distribution histograms are presented in Figure 4.3.2. Pt can be seen as light gray and black particles dispersed on XC72 in the SE and BF micrographs, respectively.

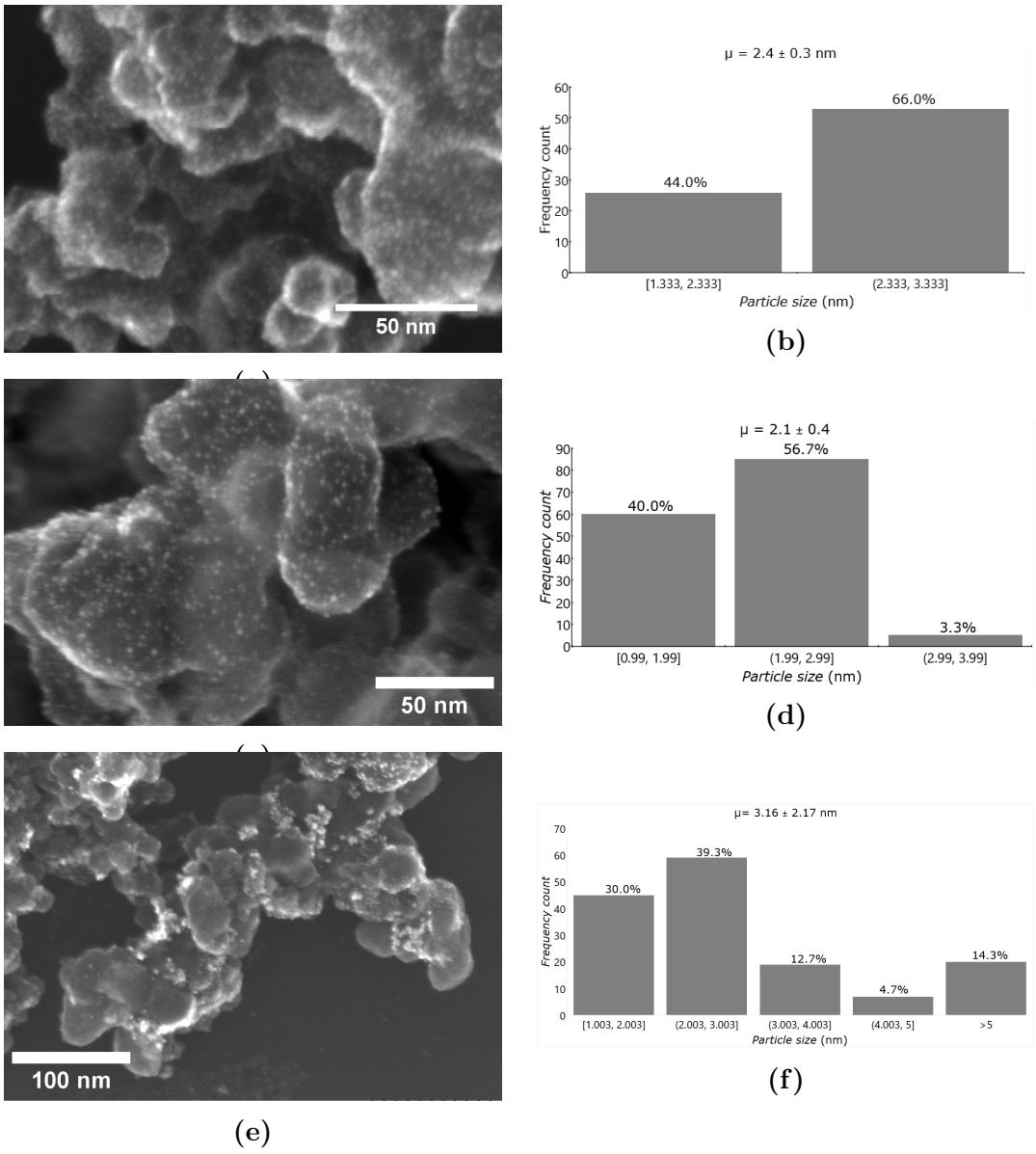

Figure 4.3.2: S(T)EM micrographs of (a), sonochemically synthesized Pt/XC72 20wt% in (200 mL)(b), and the corresponding size histogram (c), sonochemically synthesized 20wt% in (800 mL) (d), and the corresponding size histogram, (e), commercial chemically synthesized Pt/XC72 40wt%, and (f) the corresponding size histogram.

Sonochemically synthesized Pt/XC72 had a more narrow size distribution and less aggregated, more spherical particles compared to chemically synthesized Pt/XC72.

The X-ray diffractograms of Pt/XC72 are presented in Figures 4.3.3. Peaks are observed at around 39.5 °, 46.2 ° and 67.5 ° which corresponds to the (100), (200), and (220) planes of Pt, respectively, while the diffuse peak at 42° is due to carbon black. The peaks in the diffractogram of synthesis series 1 are the most pronounced. Pawley refinement revealed that the crystallite size, evaluated by Lorentzian integral breath profile shape function, is significantly larger compared to the other synthesis series. A greater occurrence of large particles in synthesis series 1 was also observed by S(T)EM and TEM imaging, as can be seen from the histogram and Figure 4.3.5b. The (100), (200), and (220) peaks were either

diffuse or absent in sample number 6 from synthesis series 2 and for all samples in synthesis series 3 and series 4. However, the presence of Pt in the samples where XRD peaks were absent was confirmed by EDS. A representative EDS spectrum is shown in Figure 4.3.4e.

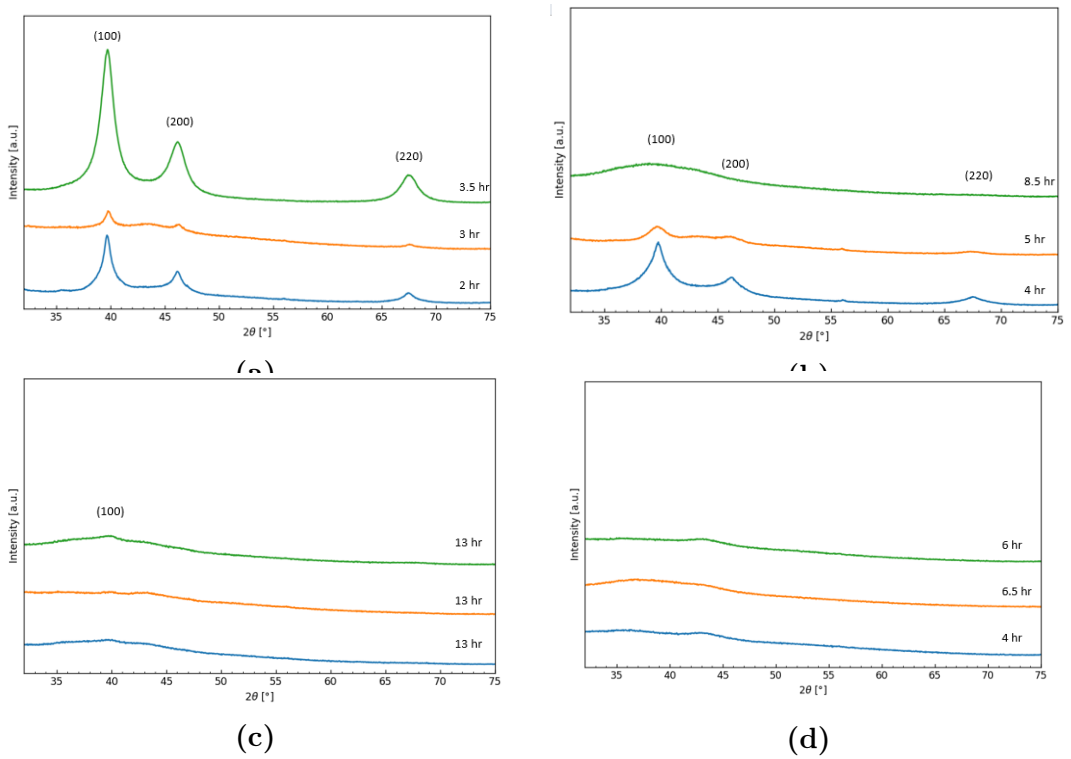

(c) (d)

Figure 4.3.3: XRD diffractograms of Pt/XC72 from synthesis series 1 (a), series 2 (b), series 3 (c), and series 4 (d).

Figure 4.3.4 shows two overview images of the same area of sonochemically synthesized Pt/XC72 20wt% obtained by secondary electron and bright field mode by S(T)EM imaging, a magnified section of the same sample and the corresponding EDS map and EDS spectrum.

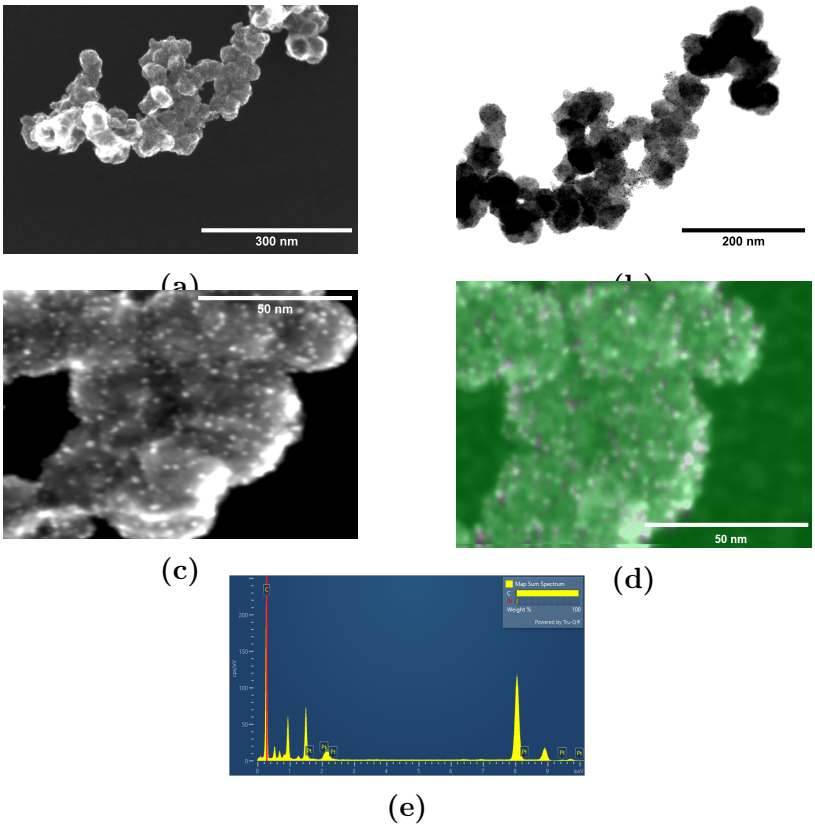

(a) (b) (c) (d) (e)

Figure 4.3.4: S(T)EM secondary electron micrograph of sonochemically synthesized Pt/XC72 20wt% overview image (a), magnified area of overview image in (a) (b), with corresponding EDS map overlaid micrograph (c), and EDS spectra (d).

Pt particles appear to be well dispersed. However, this does not necessarily reflect the dispersion of the whole catalyst. The signal from Pt is colored in magenta in the EDS map (Figure 4.3.4d). Peaks in the EDS spectra that did not correspond to Pt are signals from Al due to the S(T)EM sample holder and Cu from the S(T)EM sample grid.

Characterizarion by TEM was used as a complementary method to XRD to investigate if the increasingly diffuse and lost peaks in the XRD diffractograms (Figures 4.3.3b, 4.3.3c and 4.3.3d) were due to decreased crystallinity as a function of synthesis time as suggested in the literature [84]. Figure 4.3.5 shows TEM overview image of Pt/XC72 from sample 1 (a), the corresponding size distribution (b), a magnified image of the area enclosed in red in the overview image, and the corresponding SAED (c).

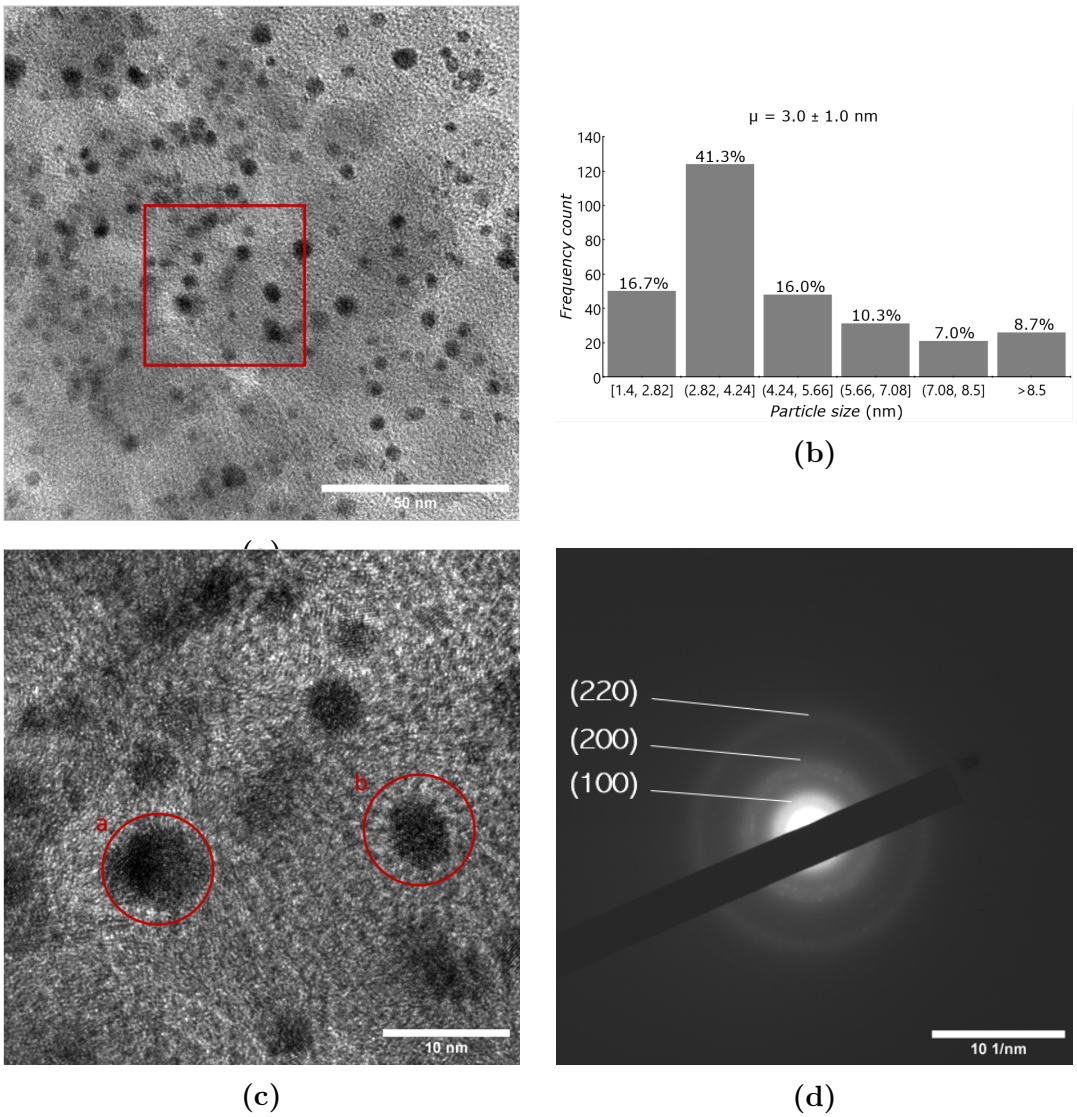

Figure 4.3.5: TEM overview image of Pt/XC72 (a), and the corresponding size distribution (b), a magnified image of the area enclosed in red in the overview image (c), and SAED (d).

The electron diffraction rings were mostly diffuse, with some spots corresponding to crystalline material. Measured d-spacings of 3.80 Å, 1.96 Å, and 1.84 Å obtained from the electron diffraction rings corresponded quite well to the theoretically calculated d-spacings of 3.91 Å, 1.96 Å, and 1.75 Å corresponding to lattice planes (100), (200), and (220), respectively. The planes indexed from observed d-spacing in TEM corresponded well to the planes that were indexed from peaks in the XRD diffractograms.

Figure 4.3.6 shows a TEM image of a Pt-particle supported on XC72 from synthesis 3, the FFT of the particle and an overview image, and a SAED of the overview area.

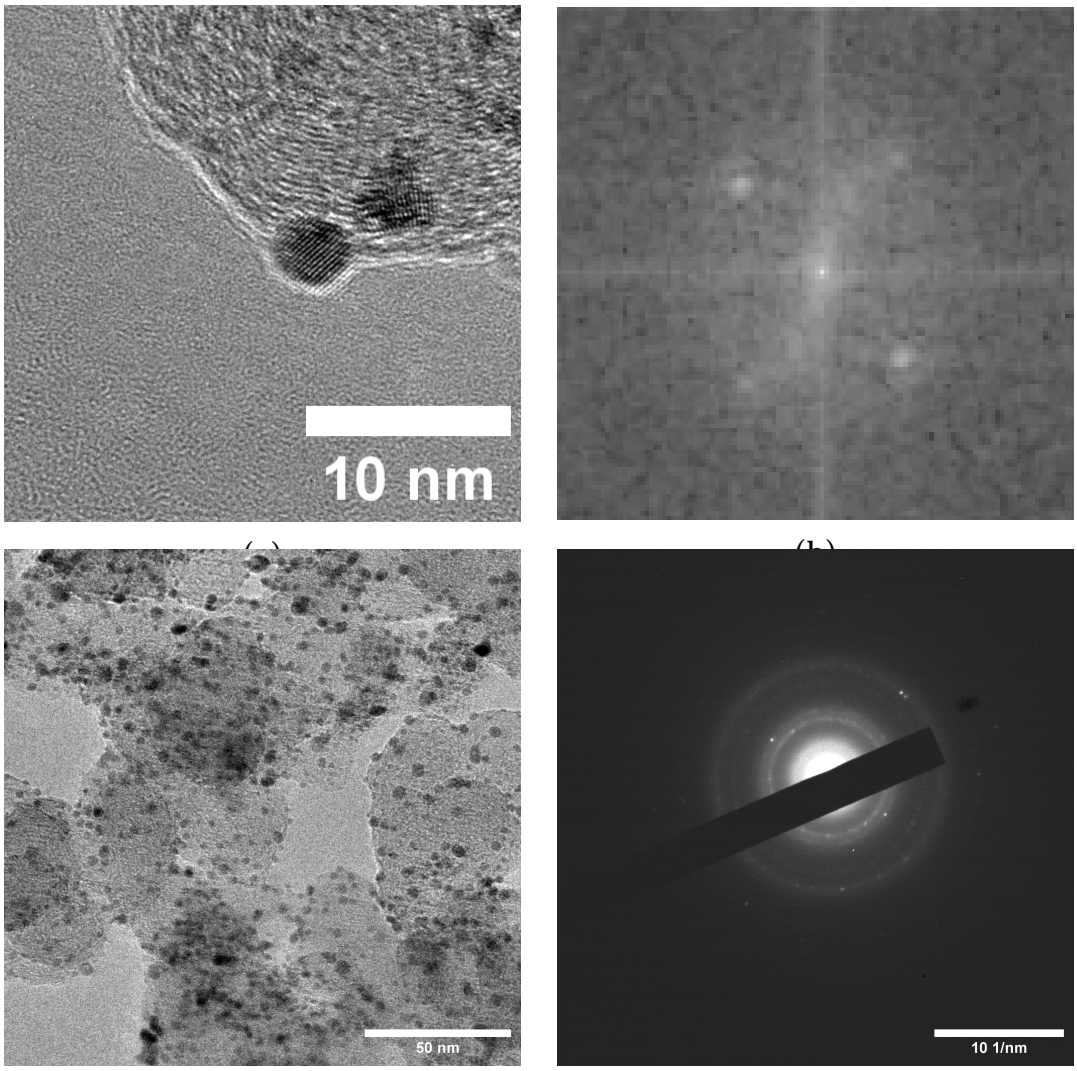

Figure 4.3.6: TEM micrograph of (a), a Pt/XC72 (b), FFT of the Pt-particle in A (c), overview image and (d), SAED of overview image.

Lattice planes were clearly observed in the Pt-particle in Figure 4.3.6a, the FFT of the particle d-spacing of 0.19 Å, the SAED in Figure 4.3.6d exhibited many diffraction spots corresponding to multiple crystalline particles in the overview image. Characterization by TEM revealed the presence of small and crystalline particles for synthesis times of 2 hours and 3.5 hours.

Figure 4.3.7 shows a TEM image of a Pt-particle supported on XC72 from synthesis 8 and a SAED of the overview area.

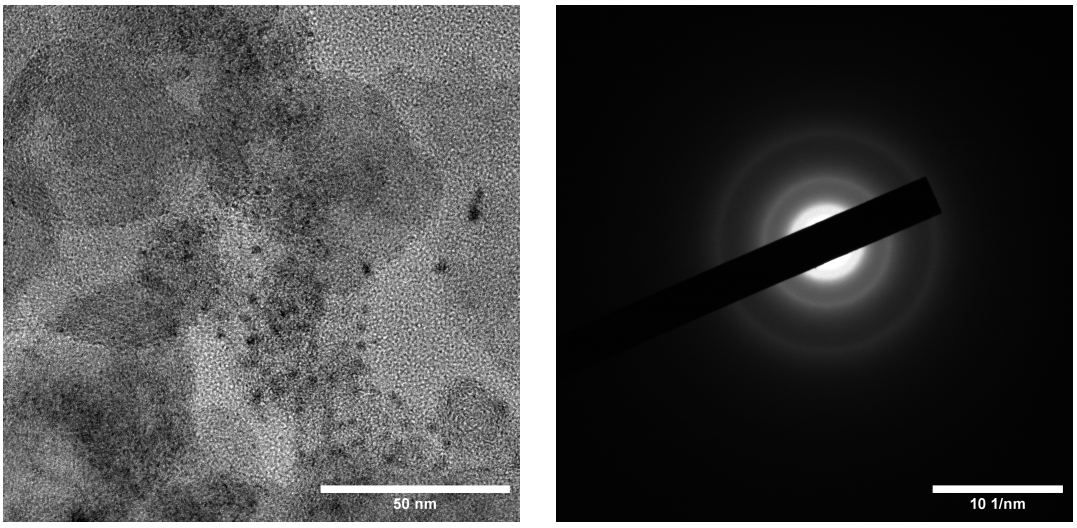

(a) **(b)**

Figure 4.3.7: TEM micrograph of Pt/XC72 (a), overview image (150K) and (d), SAED of overview image (b).

The indexing of the diffraction rings of 3.72 Å, 2.09 Å, and 1.61 Å could correspond to the Pt (100), (200), and (220) planes, however, the measured interplanar distance did not correspond as well as the synthesis 1 and 3 .

,

4.4 Catalyst Activity

Nanoparticles have large surface area-to-volume ratios, meaning that their real surface area is much larger than the geometrical area of the electrode. The observed currents are related to the catalyst activity in terms of per-site turnover by the electrochemical surface area (ECSA). Reliable materials benchmarking relies on the precise determination of surface area for an accurate comparison of electrocatalyst performance, as mentioned in section 2.3.2. Evaluation of the ECSA of Pt/XC72 was done by the hydrogen under deposition and CO-stripping voltammetric methods.

Representative cyclic voltammograms used to find the ECSA from H_{UPD} of Pt/XC72 20wt% synthesized sonochemically in a small reactor (200 mL) and a large reactor (800 mL), and a commercial chemically synthesized Pt/XC72 40wt% are presented in Figure 4.4.1.

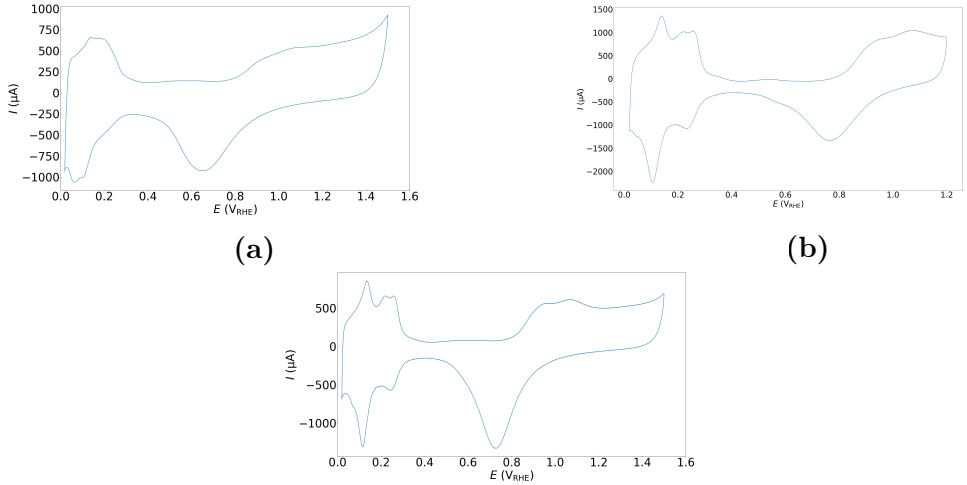

Figure 4.4.1: Cyclic voltammograms recorded from 0.2 V to 1.5 V with a scan rate of 50 mVs^{-1} at 1600 rpm in 0.5 M H_2SO_4 bubbled with Ar-gas*, of sonochemically synthesized Pt/XC72 20wt% in a 200 mL reactor (a), sonochemically synthesized Pt/XC72 20wt% in an 800 mL reactor (b), and a commercial chemically synthesized Pt/XC72 40wt% *(bubbled with N_2) (c).

The general shape of the CVs is characteristic of Pt in H_2SO_4, as can be seen from Figure 2.3.2. The peaks sonochemically synthesized of Pt/XC72 20wt% produced in the 200 mL reactor shown in Figure 4.4.2a displayed better resolution of peaks compared to Pt/XC72 20wt% synthesized in the 800 mL reactor, shown in Figure 4.4.2b. The commercial Pt/XC72 40wt% displayed the best resolution of peaks, as expected for a catalyst with higher loading and larger particle sizes.

Representative CO-stripping voltammograms of Pt/XC72 20wt% synthesized sonochemically in a small reactor (200 mL) and a large reactor (800 mL), and a commercial chemically synthesized Pt/XC72 40wt% are presented in Figure **??**, the first sweep is the CO-stripping, and the second sweep was used as a baseline of finding $ECSA_{CO}$.

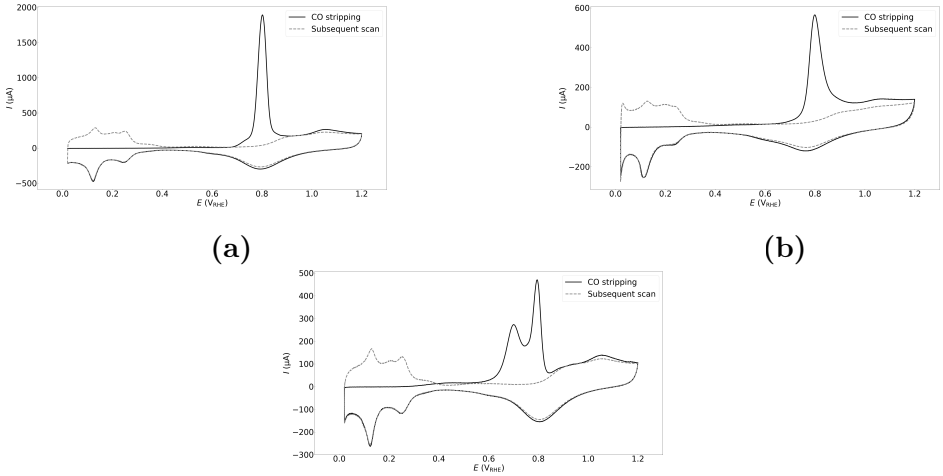

Figure 4.4.2: CO-stripping cyclic voltammograms of Pt/XC72 recorded from 0.2 V to 1.2 V with a scan rate of 10 mVs^{-1} in 0.5 M H_2SO_4. The solution was bubbled with CO-gas for 10 minutes and subsequently bubbled with N_2-gas for 30 minutes while maintaining a potential of 0.05 V. Sonochemically synthesized Pt/XC72 20wt% in 200 mL reactor (a), sonochemically synthesized Pt/XC72 20wt% in 800 mL reactor (b), and a commercial chemically synthesized Pt/XC72 40wt% (c).

The average peak CO-stripping potential was 0.80 ± 0.01 V for all 14 samples that were investigated. This suggests the complete removal of the CO adlayer on Pt [41].

ECSA for all samples was obtained from the cyclic voltammograms and CO-stripping voltammograms. The ECSA from H_{UPD} both unnormalized and normalized on TGA loading are presented in Figure 4.4.3.

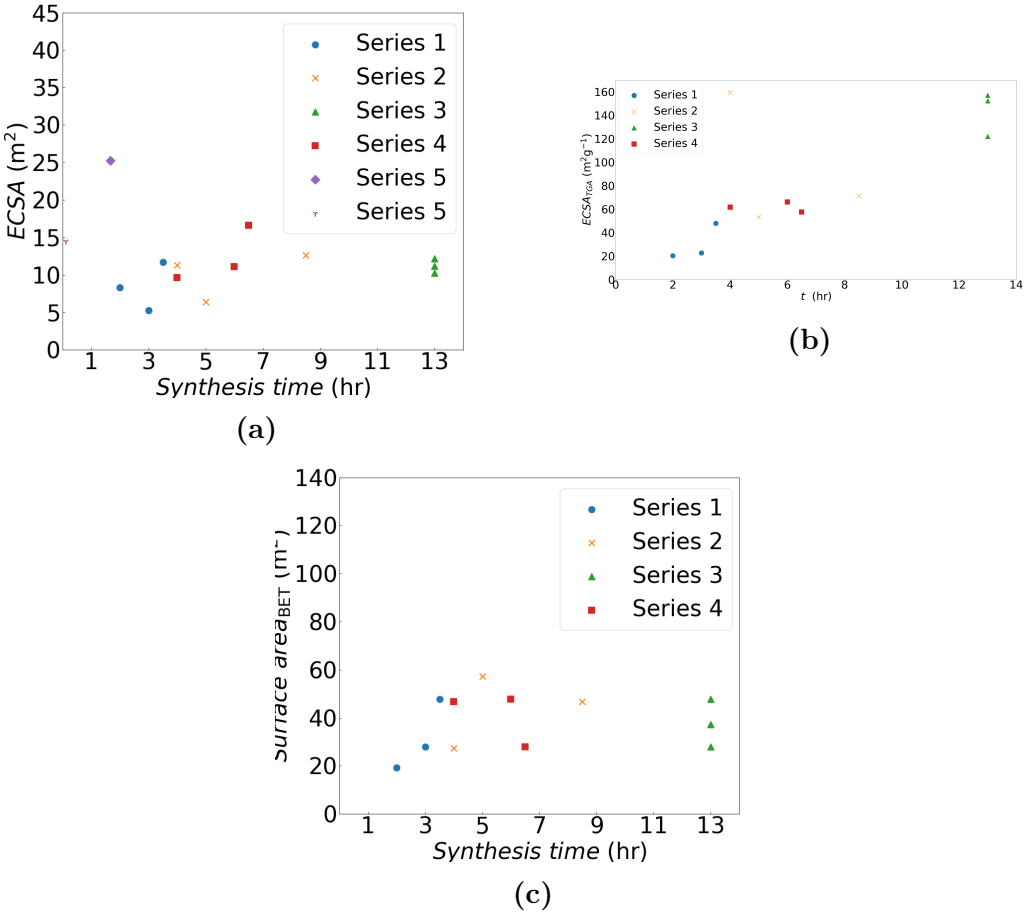

Figure 4.4.3: Surface area measurements from $ECSA_H$ (a), $ECSA_H$ normalized on TGA (b), $ECSA_{CO}$ normalized on TGA (c), $ECSA_{CO}$ normalized on TGA (d), and BET surface area (e).

As expected, ECSA tended to increase with longer synthesis time due to more Pt being formed. The surface area found by $ESCA_H$ normalized on loading was generally much higher compared $ECSA_{CO}$ values. The surface area obtained by BET was generally in better agreement with the $ESCA_H$. Some ECSA surface values become very high when normalizing on small catalyst loadings.

Polarization curves obtained by LSV were used to assess the catalytic activity of the Pt-NPs towards the hydrogen evolution reaction (HER) and the oxygen reduction reaction (ORR). The catalyst activity of sonochemically synthesized Pt/XC72 towards the HER reaction was assessed using the overpotential at $\eta_{10\ \mathrm{mA\ m^2}}$ as a benchmarking value and is presented in Figure 4.4.4.

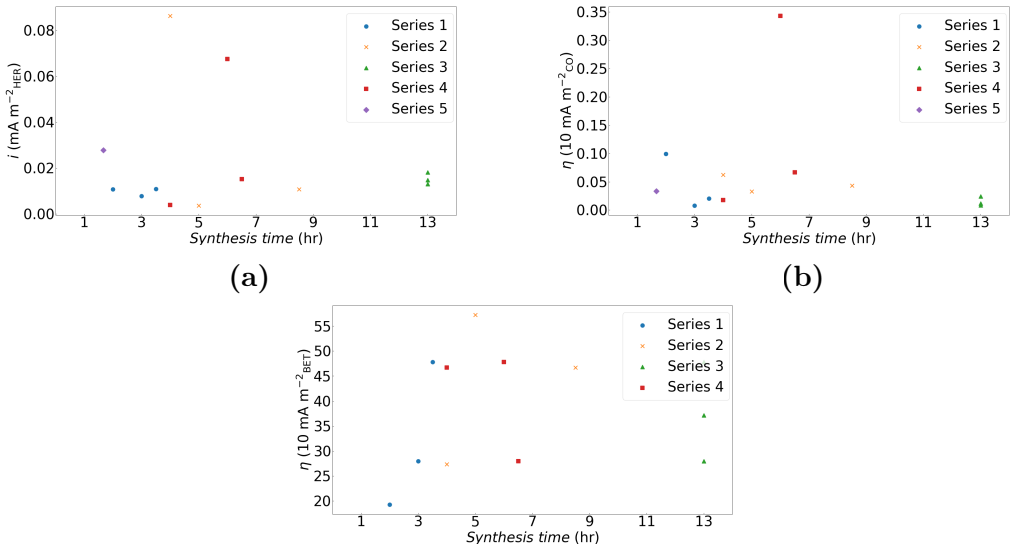

Figure 4.4.4: Catalyst activity towards HER assessed at $\eta_{10\ \mathrm{mA\ cm^2}}$ normalized on $\mathrm{ECSA_H}$ normalized on catalyst loading (a), $\mathrm{ECSA_{CO}}$ normalized on catalyst loading (b), and BET surface area.

The sonochemically synthesized XC72 generally displayed a high activity towards the HER. The activity was reproducible for various catalyst loadings determined by TGA normalized on $\mathrm{ECSA_H}$ and $\mathrm{ECSA_{CO}}$, except for synthesis number 12, which required higher overpotentials to reach 10 mA. Catalysts activity appeared to be more variable when normalizing only on the BET surface area.

The catalyst activity of sonochemically synthesized Pt/XC72 towards the ORR reaction was assessed using the overpotential at 0.9 V vs. RHE normalized on area per gram of catalyst as a benchmarking value and is presented in Figure 4.4.5.

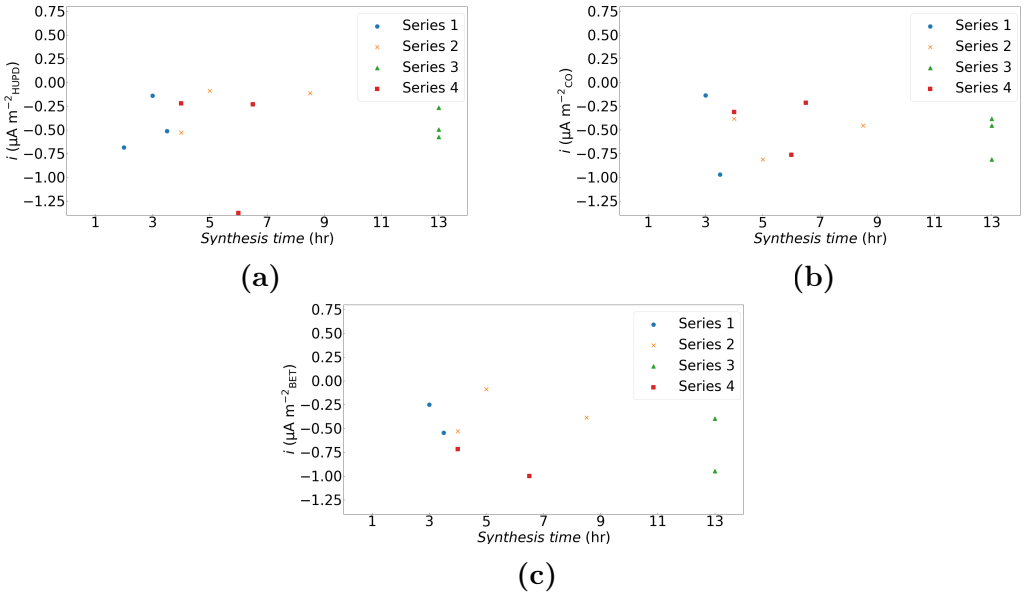

Figure 4.4.5: Catalyst activity towards ORR assessed at 0.9 V vs. RHE normalized surface area per gram of catalyst, $\mathrm{ECSA_H}$ normalized on loading (a), $\mathrm{ECSA_{CO}}$ on loading (b), and BET surface area.

The sonochemically synthesized XC72 generally displayed a high activity towards the ORR. The activity was reproducible for various catalyst loadings determined by TGA normalized on $ECSA_H$, but was more variable for normalized $ECSA_{CO}$.

CHAPTER

FIVE

DISCUSSION

5.1 Effects of Scale-Up of Reactor Volume

Increased sonochemical activity with increased reactor heights observed by sonochemiluminesence was reported by Son Y et al. as mentioned in section 2.5. Formation of a larger standing wave field with clearly separated nodal and antinodal planes with increased reactor volume (i.e., height) was also observed by similar measurements in this work (Figures 4.1.5a and 4.1.5b). Increasing the reactor height yielded a larger standing wave field which should be favorable for sonochemical activity.

However, a larger yield of radicals was not observed for an increase in liquid height but was maintained for all liquid heights (Figure 4.1.2. This could indicate increasing the height promotes the sonochemical activity for sonoluminescence but not for producing radical species. Alternatively, it could indicate that the strength of the ultrasonic field is greater over a smaller volume and weaker over a larger volume. The latter could be argued from the theory presented in section 2.4.3, which suggests that the propagation of ultrasonic waves will change to some extent by increasing the reactor height. The acoustic field can be divided into three regions. In which the first region was the one in the closest vicinity to the transducer plate, which is the lower boundary. In this region, the acoustic field has a mixed contribution of standing waves and traveling waves. The following region is the middle part of the fluid, which is not too strongly affected by the boundaries. The third region is the part near the top of the reactor, which is affected by the boundary condition implemented by the water-air interface. Increasing the liquid height will increase the separation of these three regions. SCL experiments from this work support this as there was no clear separation of sonochemically active areas in the small reactor (Figure 4.1.5a), and the upper boundary was not flat due to fountain formation. While a clear separation of a traveling wave dominated region and a standing wave dominated region was observed in the lower and mid-to-upper parts, respectively, in the large sonochemical reactor (Figure 4.1.5b), and the ultrasonic fountain height was reduced with increased reactor height. Reduced ultrasonic fountain height with increased liquid height is expected due to the lowering of the acoustic pressure by increased dampening in the large reactor caused by interactions with the reactor walls and fluid medium. Reducing the ultrasonic

fountain should promote standing waves as a flat boundary promotes coherent reflected waves and, thereby, sonochemical activity. However, the dampening of ultrasonic waves should reduce the magnitude of the negative pressures which generate cavitation bubbles and could thereby contribute to a lower sonochemical activity. Oppositely, ultrasonic waves reflected at different angles by a variable upper boundary in a small reactor can cause variable positions of the nodal and anti-nodal planes, but the reflected pressure should be stronger due to less dampening. Light can appear smeared out if it is generated at multiple variable points during an image exposure time of 30 seconds, which could also contribute to the lack of clear separation of nodal and anti-nodal planes.

Sonochemiluminesence gives a qualitative impression of how the ultrasonic field changes with increased reactor height. Due to effects that both promote and contravene sonochemical activity and without adequate instruments for detecting the emitted light intensity, one cannot conclude the quantitative effects of increasing the liquid height on the actual sonochemical activity.

Instead, quantitative investigation of the sonochemical activity for producing radicals was performed by dosimetry, combined with calorimetry, to elucidate the sonochemical efficiency (Figure 4.1.3). Increasing the reactor volume by increasing the reactor height did not significantly affect the observed acoustic power (Figure 4.1.1). The underlying assumption of the calorimetry measurement is that the only contributing factor is acoustic cavitation, as described in subsection **??**. Therefore, a constant acoustic power should indicate that the acoustic cavitation was maintained. However, the validity of the underlying assumption is known to be poor, as some electric energy is lost by being transformed into thermal energy in the piezoelectric crystal, and acoustically induced heating may contribute to the heating of the fluid, as mentioned in subsections 2.4.1 and 2.4.3. The effect of hydrostatic pressure on the dielectric loss, which causes internal heat generation in the PZT, has been found in the literature to be very small up to hydrostatic pressures of 689.48 bar [85]. The increase in hydrostatic pressure by increasing the reactor volume is therefore not thought to provide other heat contributions that would affect the acoustic power significantly. It is worth noting that the acoustic field stabilizes during the initial sonication time, which could affect the calorimetry measurements that were performed during the first two minutes of sonication. Possible contributions from multiple effects make it difficult to accurately determine the cause for the slight increase in acoustic power. However, the deviation of the average acoustic power from the mean value is moderate and corresponds reasonably well to the dosimetry measurements that indicate that radical formation is maintained within the experimental error for increased reactor volumes. It follows from the maintained rate of radical formation that the radical concentration decreased for increased reactor volume, however, when accounting for the volume. when taking the volume into account, it was found that the sonochemical efficiency was maintained within the experimental error as the rate of radical formation was maintained, and acoustic power did not change significantly.

Either the number of cavitation bubbles formed in a small-scale reactor must be approximately the same as for reactors with increased volume while also having

similar collapse conditions, or one of the reactors must have fewer bubbles with more intense collapse conditions while the other reactor must have more bubbles with less intense collapse conditions for the number of primary radicals formed to be maintained.

The reaction parameters that affect the collapse conditions (i.e., liquid temperature and ambient gas), as explained in the subsection 2.5.2, were maintained for all reactor volumes and are independent of reactor volume for this experimental set-up. The effect on collapse conditions by these parameters is therefore thought to be maintained for all reactor volumes.The frequency and power applied to the fluid affect both the number of cavitation bubbles and the collapse conditions. The effect of frequency on the collapse conditions has been found in the literature to be moderate, as presented in subsection 2.5.2. If the cavitation conditions are maintained, then the number of cavitation bubbles must be approximately the same for the radical formation to be maintained.

If the number of radicals remains constant due to the same number of cavitation bubbles being produced independent of increased reactor volume (i.e., liquid height), then the density of cavitation bubbles will decrease with increased reactor volume. It follows from this that the contributions of the secondary Bjerknes force will decrease with increased reactor volume, recalling subsection 2.4.3. If this is true, then scale-up would be favorable to reduce the quenching of the sonochemical reaction by cavitation bubble coalescence due to contributions from the secondary Bjerknes force. Increased reaction height has provided increased quenching thresholds for higher power inputs [18]. Using higher powers for scale-up reactors could be a way to increase radical formation. Scale-up of the reactor volume by increasing the height also increases the hydrostatic pressure, pushing the cavitation bubbles downwards, which possibly could promote active cavitation by contributing to positional stability in a standing wave field.

5.2 Effects of Sonication Time

Syntheses performed during the specialization project had low yields of Pt due to insufficient sonication time [31]. The rate of Pt reduction cannot be directly found from the rate of primary radical formation, as radicals formed by pyrolytic decomposition are thought to reduce Pt^{4+}, while both pyrolytic decomposition radicals and secondary radicals from primary radicals are thought to reduce Pt^{2+}. The reduction by pyrolytic decomposition was suggested to be dependent on the concentration of surfactant as mentioned in section 2.5. The effect of surfactant concentration (ethanol 96%) on the reduction of Pt^{4+} and thereby the formation of Pt^{2+} was investigated in this work. Although not directly comparable to anionic surfactants for which the CMC was the optimal concentration, it seems likely that an optimum reaction rate attained at an intermediate concentration could be due to a lack of appreciable amounts of pyrolytic decomposition product for low concentrations (i.e., less interfacially bound surfactant), while the additional mass of high concentration of interfacially bound surfactant would dampen the oscillation of the cavitation bubbles and thereby contravene acoustic cavitation.

Longer sonication times were used in this work to achieve higher product yields.

It was attempted to find system-specific sonication times based on in-situ observations of the decrease in Pt^{4+}, increase, and subsequent decrease of Pt^{2+} from UV-Vis spectra (Figure 4.2.1a and Figure 4.2.1a). Significantly faster reduction rates of Pt^{2+} were achieved for syntheses without XC72 present from the start (Figure 4.2.3. The reduced rate is attributed to the dampening of ultrasonic waves due to scattering by interactions with the XC72, which effectively hinders reducing agent formation. Reduced synthesis time, due to the removal of XC72, had a beneficial effect on the achieved catalyst loading. Significantly higher catalyst loadings were achieved for a much shorter synthesis time for synthesis series 4 and 5, in which XC72 was added near the end of the synthesis time (Figure 4.4.3c).

Literature suggested that increasing the sonication time could yield amorphous Pt-nanoparticles [84]. This was first suggested as a possible reason for the absence of diffraction peaks in the XRD diffractograms (Figure 4.3.3a , 4.3.3a , and 4.3.3a), however the experimental set-up used in this article was not comparable to this work, as they used preformed nanoparticles, pure water, a 20 kHz ultrasonic horn, and a 5 mL solution. TEM was used as a complementary method to XRD to characterize whether the particles became amorphous with a longer sonication time.

Particles from synthesis number 1, synthesized for 2 hr, had district diffraction peaks in the XRD diffractogram (Figure 4.3.3a) corresponding to (100), (200), and (220) planes. While particles from synthesis number 8, synthesized for 13 hr, had only a diffuse peak corresponding to the (100) plane. Small-angle electron scattering diffraction rings were indexed to correspond quite well to the (100), (200), and (220) planes for both short (2 hr), (3.5 hr), and long (13 hr) sonication times. Diffraction spots due to scattering from the crystalline domains were also observed (Figures 4.3.5d and 4.3.6d). The absence of diffraction spots in Figure 4.3.7b could be due to fewer particles in the overview image (Figure 4.3.7a). Lattice planes could clearly be seen in close-up images of the particles, and an FFT with distinct spots also indicated crystalline material.

The crystallinity did not appear to be affected by increased sonication time. However, the particles synthesized without XC72 present from the start had slightly smaller average particle sizes, albeit within the standard deviation of particle sizes of the other synthesis series. A slightly smaller average particle size is attributed to the faster reduction Pt^{2+} to Pt (Figure 4.2.3, which promotes nucleation over growth, as mentioned in subsection 2.7. The absence of diffraction peaks in XRD diffractograms was instead attributed to low signal-to-noise ratio and peak broadening due to crystallite and instrumental effects, which are known to be significant for characterizing nanoparticles smaller than 5 nm, as explained in subsection 2.8.1. TEM imaging revealed the presence of a subpopulation of some larger particles for synthesis number 1 (Figure 4.3.5b), which could dominate the signal in the XRD diffractograms.

Sonochemically synthesized XC72 20wt% appeared to have more spherical, less aggregated particles with a more narrow size distribution compared to commercial XC72 40wt% (Figure 4.3.2), which suggests a more homogeneous reaction

environment for sonochemical synthesis, as was observed by dosimetry (Figure 4.1.4).

The reasoning behind performing nine syntheses with XC72 added from the start was that heterogeneous nucleation was thought to be necessary for good Pt adhesion to the carbon support. At the time, one did not know what synthesis times to expect, both due to the unknown magnitude of dampening of XC72 and due to the unknown reduction rate of Pt^{4+} due to pyrolytic decomposition. The benefits of more reproducible particle properties obtained by sonochemical synthesis compared to the commercial chemically synthesized catalyst can be contravened by the long synthesis times. Further work should therefore focus on reducing synthesis time.

5.3 Catalytic Activity

Various surface area measurements were used to calculate the current density, both normalized for catalyst loading and without normalization, to avoid bias in the representation of catalyst activity (Figure 4.4.4). Most catalysts displayed a high activity towards the HER, when ECSA was normalized on catalyst loading, meaning that they required low overpotentials to reach -10 mA m^2. Reproducible performance per gram of catalyst is expected as the average particle size was reproducible (Figure 4.3.2). However, the performance was more varied when only normalizing on the surface area, which is as expected as the actual amount of Pt varied significantly, as can be seen from the TGA measurement (Figure 4.4.3c. If one had assumed that all catalysts had achieved the nominal loading of 20 wt% and judged the catalyst activity based on the surface area could, then it could have seemed as if the catalyst performance was more variable, indicating low reproducibility of the catalyst properties. This highlights the importance of the method for normalization, as mentioned in section 2.3.2. The activity of Pt catalyst toward the HER has been known to vary due to changes in experimental parameters as described in section 2.3.2. Care was taken to maintain constant experimental conditions, and the current densities were neither high nor kept long, thereby, errors from electrolyte heating should not be a contributing factor. The resistance in the solution varied somewhat but was compensated by correcting for the iR drop. The catalysts that exhibited the lowest activity towards the HER by normalization on BET had loadings and a much lower ECSA compared to the other catalyst. The RE and CE have fixed positions in the electrochemical cell. However, care must be taken to maintain a reproducible position of the working electrode.

The peak CO-stripping potential was reproducible for all samples and had an average value of 0.80 $\pm$ 0.01 V. Peak potentials at 0.80 V and overlap between the first and second sweep suggests complete removal of the CO adlayer on Pt [41]. The sonochemically synthesized Pt/XC72 displayed a high activity towards the ORR when ECSA was normalized on catalyst loading, meaning that they required low overpotentials to reach -10 mA m^{-2}. Reproducible performance per gram of catalyst was also observed for the ORR when normalizing on $ECSA_H$. Similar reproducible performance was observed when normalizing on $ECSA_H$, more varied when normalizing on $ECSA_{CO}$, due to discrepancies between the measured $ECSA_H$ and $ECSA_{CO}$. Smaller $ECSA_{CO}$ compared to $ECSA_H$ could be due to an

incomplete monolayer of CO and using a flat baseline for calculating $ECSA_H$ and using the second sweep as a baseline for calculating $ECSA_{CO}$.

5.4 Future work

Although the scale-up of this sonochemical synthesis route was successful in producing Pt/XC72, the synthesis is significantly more time-consuming compared to chemical synthesis routes using $NaBH_4$ as a reducing agent [11]. Higher revenues can be achieved for industrial-scale production by reducing synthesis time. Reducing synthesis time is beneficial for reducing operating costs associated with the wear of the components and salary expenses, as well as achieving higher product throughput. Further optimization of scale-up in the laboratory should be pursued before attempting pilot plant industrial-scale production.

The chosen frequency of 346 kHz was based on the findings from similar sonochemical synthesis routes for producing PtNP in pure water with 0.8 mol dm^{-3} ethanol 96% as a radical scavenger. It was found frequencies in the range of 210–488 kHz were optimal for producing Pt-nanoparticles with a narrow size distribution. However, this frequency range was investigated for a small reactor volume (200 mL) (i.e, shorter liquid height). This study found that increased frequencies increased agglomeration of the Pt nanoparticles [86]. However, agglomerates were not observed for Pt-nanoparticles synthesized in pure water 0.5 mol dm^{-3}, which then were dispersed on XC72 in both small and large reactor volumes (200 mL) and (800 mL). Further work could include the investigation of optimal frequency for the scale-up volume. Changing the frequency is thought to not be the most influential parameter for increasing the collapse conditions, however, changing it could be interesting for increasing the reaction rate. Frequency is, however, not an independent reaction parameter and will change the radius of the cavitation bubble, which will also affect the buoyancy and oscillation, and, thereby, also affect the secondary Bjerknes force and the available area for interfacially bound ethanol as mentioned in subsections 2.4.3 and 2.5.2. The interdependency of multiple reaction parameters makes optimization of sonochemical synthesis routes highly system specific.

A better strategy for optimization would be increasing the power input, which increases the radical formation until a quenching threshold, as explained in subsection 2.5.2. The input power should be optimized alongside the frequency. Higher radical yields can be attained for reactors with increased height as they can sustain higher power inputs without quenching the cavitation bubbles. Abrupt quenching is avoided by using a solid flat reflector at the water-gas interface, as it increases the portion of the acoustic field dominated by standing waves, which favors radical formation. A solid reflector also gives a better basis for investigating the effects of increased reactor volumes as the upper boundary condition of the acoustic field becomes comparable.

The sonochemical efficiency for producing reducing agents was maintained for scale-up reactor volumes. This could be due to a similar amount of cavitation bubbles being generated, although the ultrasonic field is affected by an increase in reactor height. Further investigation of the effect of increased reactor height

on the ultrasonic field is required to gain insight as to why the radical formation is maintained. Further work could include hydrophone experiments to investigate how the acoustic pressure changes with increased liquid height and quantification sonochemical activity by using high-speed imaging to detect the number of stable cavitation bubbles.

Significantly shorter synthesis times and increased catalyst loadings were achieved by adding XC72 in the final stages of the synthesis. Future syntheses should continue using this approach. However, it is possible that a longer sonication time with XC72 could promote better adhesion of the Pt-nanoparticles. The reproducible performance of Pt-nanoparticles and the support could be investigated by ex-situ and in-situ accelerated stress tests. Automatic catalyst spraying of the membrane should be used to achieve reproducible test conditions. Characterization of the catalyst integrity, such as the extent of particle dissolution, agglomeration, and carbon corrosion due to the imposed stress, could be investigated by electron microscopy methods.

Visual observation by S(T)EM imaging, high catalyst loadings from TGA, and catalyst behavior observed by electrochemical characterization suggested that the deposition of Pt-nanoparticles formed by sonochemical synthesis on carbon black was successful. Further work could explore the possibility of loading various types of nanoparticles on support materials, for instance, Pt-nanoparticles on carbon fibers.

Flow reactors tend to be more efficient compared to batch reactors. However, a batch reactor is preferred as stable standing waves promote acoustic cavitation. The scale-up reactor struggled to maintain isothermal conditions. Calorimetric measurements of the heat evolved during sonication should be used for calculating the necessary heat exchanger area, or the coolant flow should be increased. The placement Ar-gas supply should be optimized to avoid disturbance of the ultrasonic field. However, Ar-gas promotes high-temperature collapse conditions. Complete removal of Ar-gas is therefore not suggested. The Ar-gas flow should be controlled for better comparability between experiments.

An effective separation process scheme should be developed for industrial-scale production. From the specialization project, it was found that separation by filtering was preferred over centrifugation both in terms of time consumption and product yield [31]. If the reduction is incomplete, one could investigate the possibility of reducing the remaining Pt-ions by chemical reduction methods.

Decisions for designing industrial-scale sonochemical reactors can be made after further optimization of the laboratory scale-up reactor. Planning an industrial-scale production should involve market analysis, projecting cash flow and economic evaluation, and well as a life-cycle assessment of the product for mapping the environmental impacts. This work used a glass reactor, which was easy to disassemble. A transparent glass reactor facilitates surveillance of the equipment. Further work should be dedicated to automating the process as much as possible without introducing too many additional costs.

CHAPTER

SIX

CONCLUSIONS

Increased production volumes of Pt/XC72 catalyst with reproducible particle properties and high catalytic activity towards the HER and ORR were achieved by scale-up of this ultrasonic synthesis route, as was the desired outcome. The overall catalytic performance was greatly influenced by the catalyst loading. Shorter synthesis time and higher loading were achieved for syntheses with XC72 added towards the end of the synthesis time.

The sonochemical efficiency for producing reducing agents was maintained for scale-up reactor volumes. It was suggested that the radical formation was maintained due to approximately the same amount of cavitation bubbles being generated, although the ultrasonic field is affected by an increase in reactor height. Although the acoustic pressure will decrease due to increased dampening of the ultrasonic wave with longer propagation length, scale-up cause other effects that favor cavitation. These effects are the formation of a larger standing wave field for which cavitation bubbles can attain position stability, an increased hydrostatic pressure hindering bubbles from floating up, and a decrease in the secondary Bjerknes force, thereby decreasing bubble coalescence. Further investigation of the effect of increased reactor height on the ultrasonic field is required to gain insight into the precise mechanisms of why the radical formation is maintained. Further work could include hydrophone experiments to investigate the change in acoustic pressure with increased reactor height. High-speed imaging and cavitation bubble tracking could be used to quantify positionally stable cavitation bubbles. A solid flat reflector, such as a metallic plate, should be placed at the water-gas interface to attain similar upper boundary conditions and promote standing waves.

Reproducible nearly spherical particles with a narrow size distribution are thought to be due to the observed homogeneous reaction environment of evenly distributed radicals that were continuously generated throughout the reactor. Sonochemical synthesis offers many advantages compared to chemical synthesis routes. However, chemical synthesis is less time demanding. Further work on scale-up should concern decreasing the synthesis time. Synthesis of Pt-NP with carbon black (XC72) added at the end of the synthesis time had significantly faster reduction rates compared to syntheses in which XC72 was added at the start. Sonication time did not seem to affect crystallinity. However, faster reduction rates of Pt^{2+} lead to slightly

smaller Pt particle size. A decrease in synthesis time was achieved by attempting to optimize the radical scavenger concentration, suggesting that an intermediate concentration is preferable. However, further optimization could be attempted as only three ethanol concentrations were tested. Longer sonication time was needed reduction of Pt-ions for the scale-up reactor due to the lower concentration of radicals. Higher radical concentration can be achieved for scale-up volumes as they can accommodate higher-power inputs compared to smaller reactors (i.e., lower liquid heights). The chosen ultrasonic frequency was optimized for the small reactor (200 mL), which might not be optimal for the scale-up reactor volumes.

Various surface area measurements were used to calculate the current density, both normalized for catalyst loading and without normalization, to avoid bias in the representation of catalyst performance. Reproducible catalytic activity towards the HER and ORR reactions was achieved for most syntheses, further supporting reproducible particle properties observed by S(T)EM.

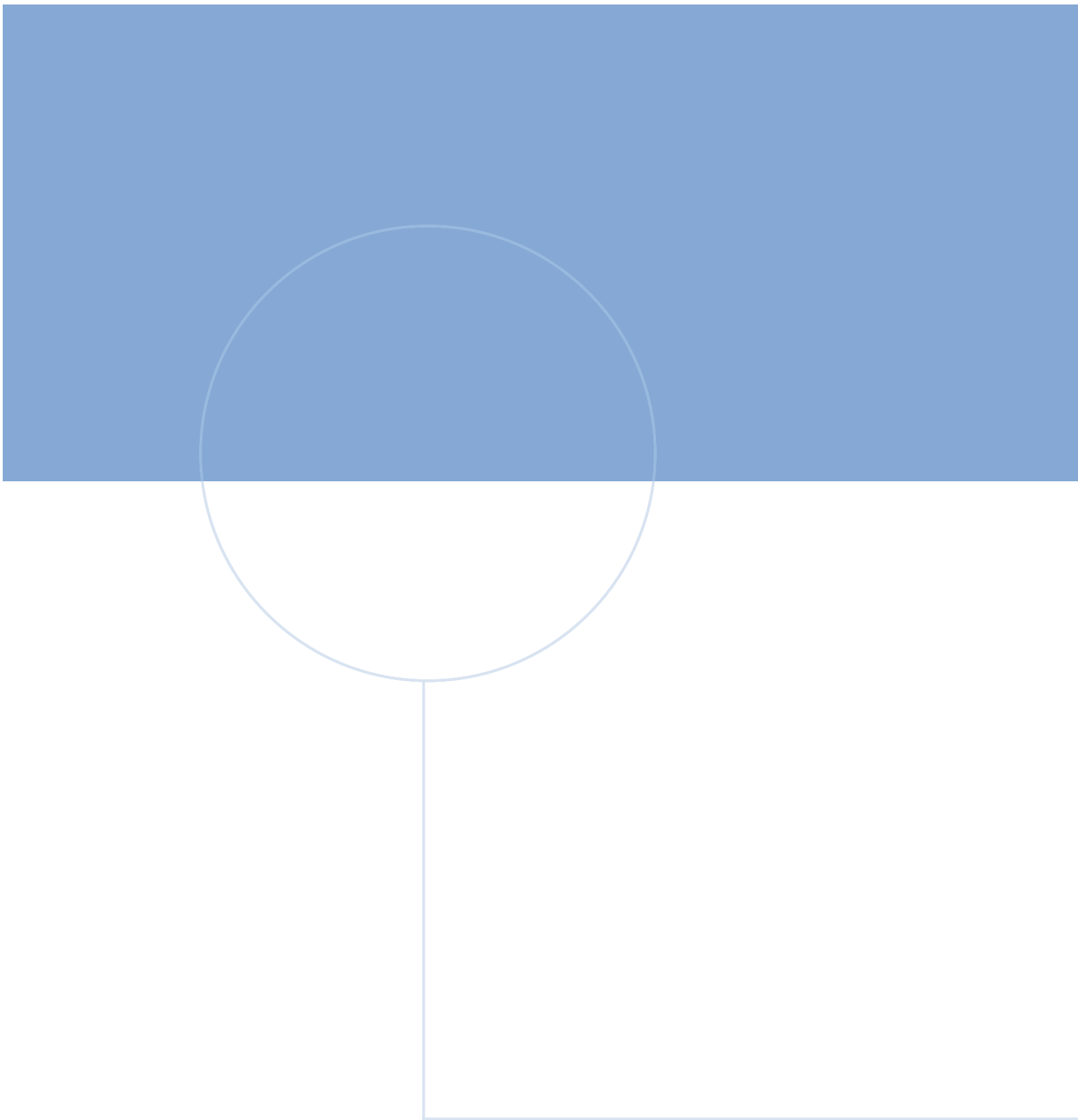

NTNU

Norwegian University of
Science and Technology